Atmospheric Research 332 (2026) 108702

Contents lists available at ScienceDirect

Atmospheric Research

journal homepage: www.elsevier.com/locate/atmosres

Influence of atmospheric parameters on the interaction between Urban Heat and Pollution Islands in a Mediterranean coastal city

A. Di Bernardino[a,*], S. Argentini[b], E. Brattich[c], M. Campanelli[b], G. Casasanta[b], A. Cecilia[b], M. Erriu[a], S. Falasca[a,d], A. Faggi[c], A.M. Siani[a]

[a] *Physics Department, Sapienza University of Rome, piazzale Aldo Moro 5, Rome 00185, Italy*
[b] *CNR, Institute of Atmospheric Sciences and Climate (ISAC), via del fosso del cavaliere 100, Rome 00133, Italy*
[c] *Department of Physics and Astronomy "Augusto Righi", University of Bologna, via Irnerio 46, Bologna 40126, Italy*
[d] *Italian National Agency for New Technologies, Energy and the Environment (ENEA), via Anguillarese 301, Santa Maria di Galeria, Rome 00123, Italy*

ARTICLE INFO

Keywords:
Urban pollution island
Urban heat island
Atmospheric pollution
Weather conditions
Heatwaves
Mediterranean

ABSTRACT

Urban Heat Island (UHI) and Urban Pollution Island (UPI) processes shape urban climate and air quality, yet their interaction remains insufficiently quantified, particularly in Mediterranean coastal cities. Existing research often examines these phenomena separately or over short time spans, leaving uncertainties regarding the meteorological drivers governing the UHI-UPI co-evolution. This study provides a multi-year, observation-based assessment of the coupled dynamics between Urban Heat Island Intensity (UHII) and Urban Pollution Island Intensity (UPII) in Rome (Italy), focusing on the atmospheric conditions that modulate their relationship. Air temperature, humidity, and wind speed, together with major air pollutants (PM_{10}, $PM_{2.5}$, NO_2, NO, and O_3), were analysed using an integrated statistical framework. Lag-correlation analysis revealed that the strongest UHII-UPII relationship occurs when nocturnal UHII is shifted backward by one day, reflecting daytime pollutant accumulation and nighttime trapping. Regression results highlighted daily mean air temperature and wind speed as the primary drivers modulating the UHII-UPII association. Spearman correlations showed negative associations between UHII and NO (−0.60), PM_{10} (−0.45), NO_2 (−0.35), and $PM_{2.5}$ (−0.34), alongside positive correlations with O_3 (0.54) and NO_2/NO (0.42). These correlations intensified during heatwaves and calm wind conditions, suggesting enhanced interactions under extreme weather and stagnant atmospheric conditions. UHII peaks in summer, while UPII maximizes in winter for all pollutants except for O_3, which exhibits an opposite pattern. These findings reveal a complex interplay between urban warming and pollutant accumulation, highlighting the need for integrated urban planning to address joint UHII-UPII challenges under ongoing urbanization and intensifying severe heat episodes.

1. Introduction

Urban Heat Island (UHI) and Urban Pollution Island (UPI) are key urban climate phenomena that significantly affect local meteorology and air quality (Chapman et al., 2017). UHI refers to the characteristic overheating of the urban atmosphere with respect to rural surroundings (Oke et al., 2017), while UPI describes the elevated concentrations of air pollutants typically observed in cities compared to the rural surrounding areas (Crutzen, 2004). To quantitatively describe these phenomena, the Urban Heat Island Intensity (UHII) measures the air temperature difference between urban and rural sites, whereas the Urban Pollution Island Intensity (UPII) quantifies the difference in pollutant concentrations between urban and rural locations.

The canopy-layer UHI arises from land surface modifications, reduced vegetation, and anthropogenic heat emissions (Oke et al., 2017). UHII negatively affects human health (Heaviside et al., 2017), thermal comfort (Falasca et al., 2023), and the environment (Čeplová et al., 2017). Depending on local climate, UHII is typically more pronounced during nighttime, warm periods, and under anticyclonic weather regimes (Oke et al., 2017). In some extreme cases, nighttime UHII values may exceed 10 °C (Kikon et al., 2016; Geletič et al., 2019), with local climatic drivers, such as wind speed and absolute humidity, playing a critical role (Kousis et al., 2021). Kong et al. (2025) showed that wind speed significantly modulates UHII in coastal cities,

---

* Corresponding author.
E-mail address: annalisa.dibernardino@uniroma1.it (A. Di Bernardino).

https://doi.org/10.1016/j.atmosres.2025.108702
Received 17 October 2025; Received in revised form 2 December 2025; Accepted 13 December 2025

highlighting the mitigating effect of sea breeze. Similarly, Morris et al. (2001) found for Melbourne (Australia) that UHII scales inversely with approximately the fourth root of both wind speed and cloud cover. Lokoshchenko and Alekseeva (2023) reported statistically significant correlations between UHII and both cloud cover and surface air temperature in Moscow (Russia), with a slightly weaker, yet non-negligible, role of wind speed and relative humidity.

In parallel, the higher concentrations of air pollutants typically observed in urban areas relative to their rural counterparts result from the dense clustering of emission sources and the generally less favourable atmospheric dispersion conditions that characterize urban environments (Crutzen, 2004). Since UPI negatively affects the life quality of urban dwellers, the revised European Ambient Air Quality Directive (EU Directive 2024/2881) established the limit concentration of ground-level atmospheric harmful substances typically present in the urban area, also including particulate matter (PM_{10} and $PM_{2.5}$, i.e., particles with aerodynamic diameter smaller than 10 μm and 2.5 μm, respectively), and gaseous pollutants, such as nitrogen oxides (NO and NO_2), and ozone (O_3). Standardized methodologies for UPII evaluation are still lacking, particularly in areas with sparse monitoring networks or episodic rural emissions. Furthermore, previous studies typically rely on single or very few stations or short-term datasets. For example, Li et al. (2018) analysed UPII in Berlin (Germany) using in-situ aerosol measurements and satellite data during the summers of 2010–2017. Bakaeva and Le (2022) combined satellite data with ground-level observations to quantify $PM_{2.5}$-related UPII in Moscow (Russia). Similarly, Hereher et al. (2022) assessed seasonal UPII patterns from 2018 to 2021 using nocturnal surface UHII and air pollutant distributions derived from satellite observations.

Despite a growing interest in the atmospheric drivers and their impacts on UHI and UPI, these complex phenomena are often examined disjunctively. However, increasing evidence highlights a strong interconnection between them, with meteorological conditions and atmospheric dynamics playing key roles in modulating their relationship (Ulpiani, 2021). In fact, high urban air temperatures can enhance turbulent mixing and deepen the urban boundary layer, thereby facilitating pollutant dispersion and lowering near-surface concentrations (Battista and de Lieto Vollaro, 2017). At the same time, the reduction of the vertical mixing and the concomitant increase of primary pollutants are side effects of the UHI mitigation techniques (Fallmann et al., 2016). Conversely, particle accumulation, particularly of $PM_{2.5}$, can intensify nocturnal UHII by increasing atmospheric longwave radiation trapping (Li et al., 2018), as also demonstrated by Cao et al. (2016), who found that this feedback can raise nighttime UHII by up to 0.7 °C in several Chinese cities. This loop may exacerbate the process, as higher urban temperatures lead to increased demand for cooling systems, which in turn leads to an increase in energy consumption and anthropogenic emissions, further amplifying both UHII and UPII (Roxon et al., 2020). In addition, simulation-based studies have further explored the interplay between urban heat generation due to anthropogenic activities and its impact on UHI and UPI. For example, Matak and Momen (2025) demonstrated that UHI effects influence planetary boundary layer dynamics, enhancing urban air pollution forecasts. Similarly, Zhong et al. (2018) investigated the urbanization effect on winter haze in the Yangtze River Delta, showing that anthropogenic heat and emissions exacerbate pollutant accumulation and intensify the UHI-UPI interactions. These simulation-based results complement ground-based observational studies, emphasizing that anthropogenic heat release and emissions not only intensify UHI but also modulate pollutant accumulation, thereby influencing UPI dynamics. This mechanistic perspective helps to explain observed patterns and provides a link between urban climate processes and air quality outcomes under varying meteorological conditions.

Despite the Mediterranean region being widely recognized as a climate-change hotspot (Nastos and Saaroni, 2024), its urban environments remain comparatively understudied with respect to the coupled dynamics of UHI and UPI. In this context, few studies have quantitatively examined their joint behaviour over multiple years using ground-based observations. Moreover, existing research has largely focused on exploratory analyses, without systematically evaluating the meteorological drivers that modulate the UHII-UPII relationship or examining its variability during peculiar atmospheric events. This study addresses these gaps by combining a multi-year observational dataset with rigorous statistical analyses and event-based classification, providing a more detailed understanding of how urban warming and air pollution accumulation interact across different seasons and meteorological conditions. By identifying the key meteorological drivers influencing the UHII-UPII association and assessing its behaviour during distinct atmospheric events, the present work offers new insights into the mechanisms governing urban climate and air quality, which are critical for supporting effective mitigation and adaptation strategies (Baklanov et al., 2016).

Specifically, the present study aims to contribute to the understanding of the coupled role of UHII and UPII by pursuing the following objectives: (i) to characterize the spatial-temporal variability of UHII and UPII using a multi-year observational ground-based dataset for the urban area of Rome (Italy); (ii) to identify the meteorological variables that most significantly affect the UHII-UPII relationship through comprehensive statistical analyses, including multiple linear regression; and (iii) to quantify the UPII-UHII functional relationship evaluating correlations, also under various meteorological conditions, including the co-occurrence of multiple specific events, providing insight into how extreme or unusual weather patterns modulate their coupling.

The remaining sections of this paper are structured as follows: Section 2 describes the study area, and the air quality and meteorological datasets used. Section 3 outlines the adopted methodology, focusing on the statistical tools and event classification criteria. Sections 4 and 5 present and discuss the results, respectively. Finally, Section 6 summarizes the main outcomes of the study.

2. Study area and datasets

This section outlines the main geographical, meteorological, and environmental characteristics of the area under investigation. In addition, it presents the observational datasets employed for the analysis of UPII and UHII, describing the spatial distribution and classification of the air quality monitoring stations, the meteorological observations network, and the temporal coverage of the data considered.

2.1. Study area

The area under investigation is the city of Rome, the capital of Italy, located in the central-western portion of the Italian Peninsula (41.9° N, 12.5° E, Fig. 1), approximately 27 km inland from the Tyrrhenian Sea. The metropolitan area, characterized by the alternation of highly urbanized zones and urban parks, has a complex and heterogeneous orography, with the Apennines to the east gently descending towards the coast of the Tyrrhenian Sea to the west. The Tiber River, which bisects the city from north to southwest, flows through a narrow valley and plays a central role in shaping both the urban morphology and atmospheric circulation patterns within the city. In fact, during daytime, especially in the case of sunny days and under high-pressure conditions, the air temperature gradient between the inland and the offshore determines the onset of the sea breeze, which often begins late in the morning and penetrates up to the city centre between 10:00 and 12:00 LT, also modulating urban boundary layer development (Di Bernardino et al., 2021). On the contrary, a weak northeasterly drainage flow, associated with land breeze or katabatic flows descending from the surrounding hills (Petenko et al., 2011), develops during the night and early morning. Mean wind speeds are relatively low year-round (typically $\leq$2 m/s), and synoptic-scale subsidence is frequent during summer, suppressing vertical mixing and, in combination with weak inland

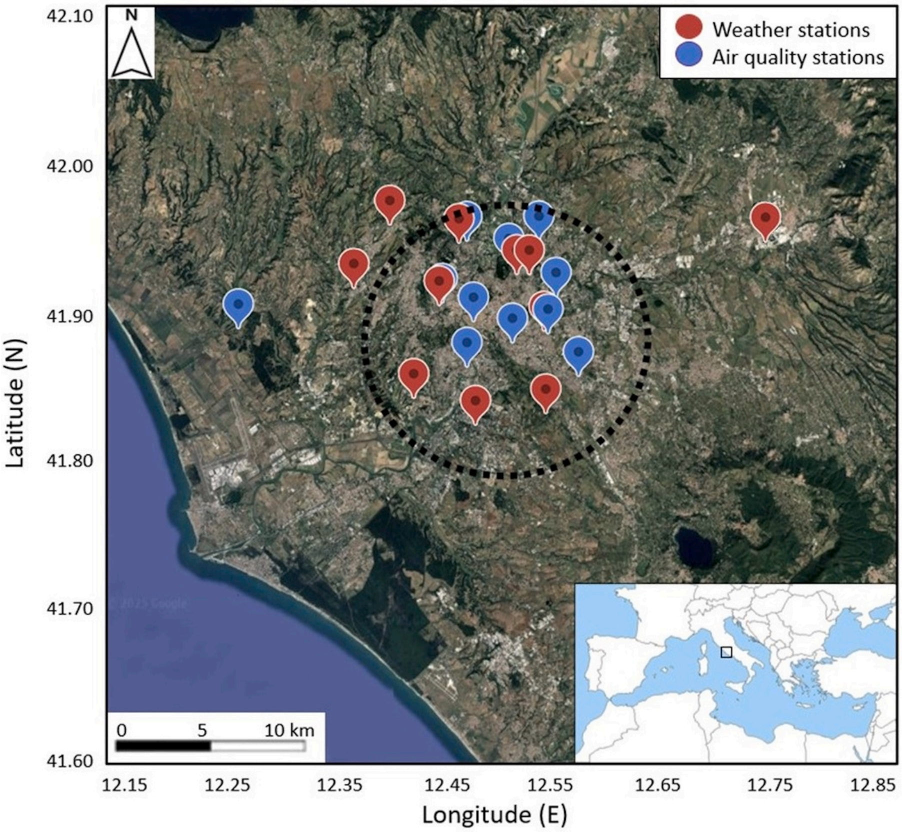

Fig. 1. Geographic map of the region under investigation. The black dotted line identifies the urban area of Rome, blue markers depict the location of the air quality stations listed in Table 1, and red markers show the location of the meteorological stations summarized in Table 2. (For interpretation of the references to colour in this figure legend, the reader is referred to the web version of this article.)

winds, leading to stagnant conditions that exacerbate both heat and pollution accumulation, particularly in low-lying urban basins (Guattari et al., 2018). According to the Köppen–Geiger climate classification, Rome belongs to the Mediterranean climate (Csa), experiencing hot, dry summers and mild, wet winters (Beck et al., 2018). Unlike other major European cities, Rome lacks significant heavy industrial plants within its urban perimeter, and the main economic activities are related to the tertiary sector. This implies that the air pollutants detectable in downtown Rome are mainly due to local anthropogenic emission sources, such as road traffic, domestic heating, and commercial activities, rather than to the regional advection (Perrino et al., 2009). In addition, the city is frequently affected by long-range transport of Saharan desert dust across the Mediterranean basin. These episodes can lead to a significant increase in the atmospheric particulate matter loads and exceedances over the region, with implications for air quality and radiative forcing (Gobbi et al., 2013).

Rome's distinctive topography, coastal proximity, and urban characteristics, combined with its location in the middle of the Mediterranean basin, make it an optimal case study for examining the interactions between urban climate and air quality in coastal cities. The Mediterranean region is widely recognized as a climate-change hotspot, hosting some of the world's most densely populated and rapidly expanding urban areas. Because daily life in this region is largely conducted outdoors, residents are increasingly exposed to a progressively harsher climate and more frequent extreme weather events (Nastos and Saaroni, 2024), underscoring the need to understand how local urban processes, such as UHI and UPI, evolve in this environment.

2.2. Air quality dataset

All air quality data used in this study to assess UPII are collected from the air quality monitoring network operated by the Regional Agency for Environmental Protection of Lazio (ARPA Lazio). The analysis focuses on daily-averaged concentrations of particulate matter fractions (PM_{10} and $PM_{2.5}$), as well as the hourly-averaged concentrations of gaseous pollutants (NO_2, NO, and O_3), collected over the period 01/01/2019–31/12/2023. The time frequency for the species is consistent with the European Ambient Air Quality Directive mentioned above. All air quality measurements were conducted at a height of 3.5 m above ground level (personal communication from ARPA Lazio). The dataset includes observations from eleven ground-based monitoring stations, of which ten are located within the urban area of Rome, capturing a range of emission and land-use characteristics typical of the metropolitan area. The remaining station is located in a rural area west of the city, within an agricultural zone. Its location within a predominantly rural landscape ensures that local pollutant levels are minimally influenced by nearby emission sources, making it a suitable reference for evaluating differences between urban and rural air quality. Being the only rural background air quality monitoring station in the vicinity of Rome, this site has been selected as the reference location for evaluating differences in pollutant concentrations between urban and rural environments. Di Bernardino et al. (2025) previously employed the same air quality observation station dataset to evaluate UPII in the metropolitan area of Rome. Fig. 1 depicts the geographical distribution of the air quality monitoring sites (represented by blue markers), while Table 1 provides a detailed overview of each site's location and the monitored pollutants.

In addition to the air pollutants' concentrations directly measured by the in-situ air quality stations, the NO_2 to NO ratio was computed, as it is commonly used in the literature as a proxy for estimating the photochemical age of air masses (Tseng et al., 2009; Rowlinson et al., 2025). Fresh anthropogenic emissions typically contain both primary NO_2 and NO, while photochemically aged air masses contain lower

Table 1
List and details of air quality monitoring stations considered in the present study.

Station ID	Lat. (° N)	Lon. (° E)	Elevation (m a.s. l.)	Monitored variables
ARPA-02	41.89	12.54	37	PM_{10}, NO_2, NO, O_3
ARPA-03	41.95	12.47	43	PM_{10}, $PM_{2.5}$, NO_2, NO
ARPA-05	41.88	12.51	49	PM_{10}, NO_2, NO
ARPA-08	41.86	12.57	53	PM_{10}, $PM_{2.5}$, NO_2, NO, O_3
ARPA-39	41.93	12.51	50	PM_{10}, $PM_{2.5}$, NO_2, NO, O_3
ARPA-40	41.89	12.27	61	PM_{10}, $PM_{2.5}$, NO_2, NO, O_3
ARPA-47	41.87	12.47	26	PM_{10}, NO_2, NO
ARPA-48	41.95	12.53	41	PM_{10}, NO_2, NO, O_3
ARPA-49	41.91	12.45	31	PM_{10}, $PM_{2.5}$, NO_2, NO, O_3
ARPA-55	41.91	12.55	32	PM_{10}, NO_2, NO
ARPA-56	41.89	12.47	31	PM_{10}, $PM_{2.5}$, NO_2, NO, O_3

concentrations of NO, which tends to be rapidly oxidized by ozone in the atmosphere, forming secondary NO_2, thus enhancing the ratio (e.g., Tremmel et al., 1998). Accordingly, high NO_2/NO values suggest photochemically aged air masses, while low ratios are indicative of fresh and local emissions.

2.3. *Meteorological dataset*

Meteorological data are collected from in-situ rooftop measurements at 10 weather stations, shown by the red markers in Fig. 1. These stations belong to the ASTI-Network, established within the framework of the LIFE-ASTI project (https://lifeasti.eu, last accessed on 02 December 2025). The network integrates stations from the Meteo Lazio amateur network (https://meteoregionelazio.it, last accessed on 02 December 2025), as well as additional stations installed specifically by the Institute of Atmospheric Sciences and Climate (branch of Rome) of the National Research Council of Italy (CNR-ISAC) to fill data gaps in uncovered areas (Cecilia et al., 2023). All selected stations are Davis Vantage Pro 2 (Davis Instruments Corp., Hayward, CA, USA) and are chosen to ensure data coverage by exceeding 90 % of the study period. Each station records air temperature, relative humidity, and wind speed at 10-min intervals, and the data were subsequently daily aggregated to ensure comparability with the air-quality measurements. Note that station ML-44, situated just outside the Rome urban area, was used exclusively to identify cold-pooling nights. Owing to its location within the Aniene River valley, the site undergoes pronounced nocturnal cooling under favourable meteorological conditions, exhibiting a marked temperature drop relative to stations not influenced by cold-air drainage. This makes ML-44 particularly suitable for detecting cold-pooling events through nighttime temperature differences between the two sites.

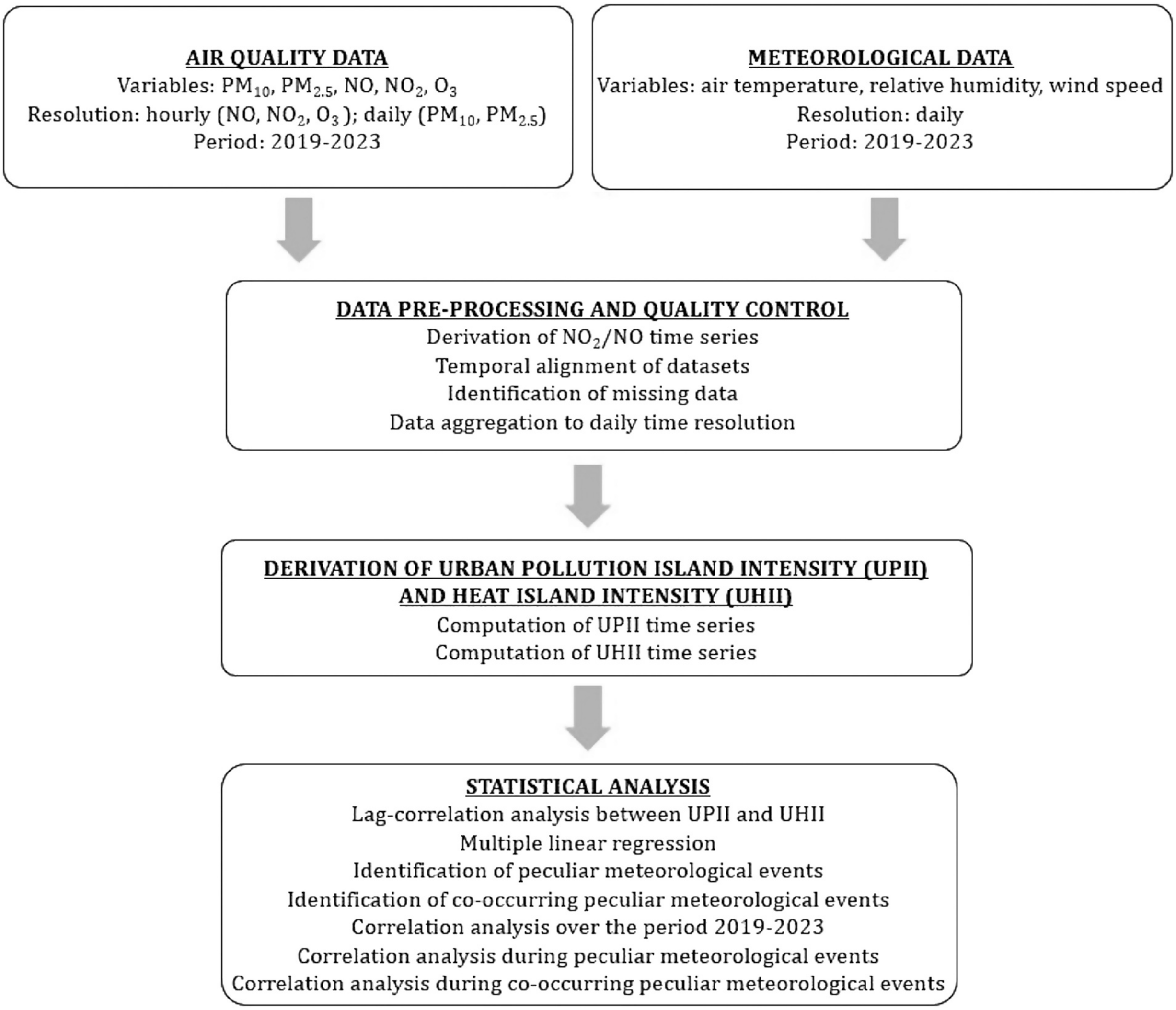

Fig. 2. Schematic diagram of the adopted methodology to investigate the interaction between thermal and air pollutants urban-to-rural differences.

3. Methodology

This section presents a comprehensive description of the analytical procedures adopted to investigate the relationship between UPII and UHII in Rome. The overall structure of the analysis is depicted in Fig. 2, which presents a step-by-step overview of the workflow and is further explained in the subsequent subsections.

3.1. Assessment of UHII and UPII

The UHII is assessed using the imperviousness method, which assumes a linear relationship between air temperature and imperviousness (IMP) (Cecilia et al., 2023). This latter parameter represents the percentage of an area covered by artificially sealed surfaces, such as roads or buildings. It ranges from 0 % to 100 % with 1 % increments and is provided at a 10 m spatial resolution by the Copernicus Land Monitoring Service (Copernicus, 2018). IMP associated with each meteorological station was calculated as the average of the values within a circle of radius $r = 1400$ m centred on the site, a spatial scale identified by Cecilia et al. (2023) as the footprint of a weather station in the urban context of Rome. Each station, therefore, is associated with a distinct IMP value, depending on its surroundings. For each time step of the dataset, a linear regression was carried out using the relationship:

$$\mathrm{T}(\mathrm{IMP}, t) = a(t)\cdot\mathrm{IMP} + b(t) \tag{1}$$

where t denotes the time. In this framework, the slope $a(t)$ represents the intensity of the air temperature–imperviousness relationship at time t. According to the method used to estimate UHII, defined as the temperature difference between fully urbanized areas (100 % IMP) and rural areas (0 % IMP), the UHII at time t corresponds to $100\cdot a(t)$. Here, the UHII was computed at an hourly resolution from the input meteorological dataset and subsequently averaged over the nighttime period (22:00–06:00 CET) for each day. This temporal window was selected following Cecilia et al. (2023), who identified it as the interval during which the UHI is fully developed within Rome's urban canopy layer—even during summer, when nights are shorter. Their analysis, conducted on the same stations used in this study, showed that daytime UHII values were negligible and that the correlation between air temperature and imperviousness was not statistically significant. In contrast, during nighttime hours the UHI was consistently present, with a strong correlation ($R = 0.81$) and a relatively stable temporal evolution once established. As a result, moderate changes in the exact nighttime boundaries would not substantially alter the UHII estimate, provided that only hours in which the UHI is active and fully developed are included. The same behaviour was confirmed in the current dataset, where significant correlations ($R > 0.6$) were found exclusively during nighttime hours. Including daytime values would therefore introduce noise and lack physical justification, as the fundamental assumption of the estimation method (a linear relationship between temperature and IMP) does not hold during the day. For these reasons, UHII in this study is defined solely from its nighttime average, which captures the period when the phenomenon is active and reaches its maximum intensity. This choice remains fully compatible with the use of daily averages for UPII, as the purpose is to analyse its relationship with UHII during the hours when the latter actually occurs.

The UPII is computed following the methodology proposed and validated by Di Bernardino et al. (2025) for the same study area. This approach enables the quantification of the UPII for the i-th pollutant as:

$$\mathrm{UPII_i} = \frac{1}{n}\sum\nolimits_{j=1}^{n} c_{urb,i,j} - c_{rur,i} \tag{2}$$

where $c_{urb,i,j}$ represents the concentration of the i-th pollutant measured at the j-th urban station (with n being the total number of urban monitoring sites) and $c_{rur,i}$ is the concentration of the i-th pollutant measured at a reference rural station, considered representative of the regional background pollution level (see Sect. 2.2). Furthermore, in order to construct homogeneous time series for UHII and UPII, hourly concentrations of NO, NO_2, and O_3 were averaged on a daily basis to enable comparison with daily mean datasets. By applying this formulation, a time series of daily UPII values is obtained. This allows for a realistic and robust characterization of the pollution urban-rural difference. Note that UPII is calculated only when measurements from both urban and rural environments are available for the same day, in order to avoid temporal bias.

3.2. Investigation of the UPII-UHII relationship

The UHII and UPII time series exhibited over 95 % temporal coverage during the period 2019–2023. Missing data were randomly distributed throughout the study period and were imputable to occasional instrument maintenance or temporary malfunctions. To explore the relationship between UPII and UHII, a synergistic approach integrating multiple statistical techniques was applied, including lag-correlation analysis, multiple linear regression, and correlation analysis, as detailed below.

3.2.1. Lag-correlation and correlation analysis

To investigate the presence of a possible temporal offset in the relationship between UPII and UHII, the lag-correlation analysis is performed. The lag-correlation approach is specifically selected because UHII and UPII are driven by processes that may peak at different times of the day, making a temporal offset physically plausible. Unlike standard regression or correlation techniques, lag-correlation allows for the detection of monotonic associations occurring with a delay, without assuming linearity or normality of the data. This makes it particularly suitable for identifying short-term temporal shifts in the UHII–UPII relationship, which may arise from the combined effects of atmospheric dynamics, radiative processes, and emission patterns. This approach has been adopted to highlight temporal lags in the correlation among meteorological variables (Guan et al., 2007) and to analyse the association among particle number size distributions, gaseous pollutants, and meteorological parameters (Wehner and Wiedensohler, 2003). More recently, it was applied to study the effect of weather on cyanobacterial bloom (Wang et al., 2023) and the relationship between weather, atmospheric pollution, and human health (Ziadé et al., 2021; Jiang et al., 2024).

In this study, since the data are not normally distributed, the Spearman rank correlation coefficient is computed instead of the more common Pearson correlation coefficient (Hauke and Kossowski, 2011). This formulation permits the assessment of the monotonic relationship between UPII and UHII by comparing the ranked values rather than their absolute magnitudes, allowing for the identification of potential time delays between the two phenomena. A temporal window of ±30 days was adopted as it represents a suitable balance between capturing the temporal dynamics of the processes under study and minimizing the influence of longer-term climatic fluctuations. A time step τ of one day is considered and, for each lag τ (onward and backward), the Spearman correlation coefficient $\rho(\tau)$ is calculated as:

$$\rho(\tau) = 1 - \frac{6\sum_{i=1}^{n} d_i^2}{n(n^2-1)} \tag{3}$$

where n is the number of paired observations and d_i is the difference between the ranks of UPII and lagged UHII values for the i-th observation. Values of $\rho(\tau)$ range between -1 and $+1$. Positive values identify direct monotonic association, while negative values indicate inverse monotonic association. The maximum value of $\rho(\tau)$ highlights the temporal offset that yields the strongest correlation between UPII and UHII. Possible time lags might be attributable to different responses of UPII and UHII to atmospheric processes, such as atmospheric dynamics, photochemical processes, and weather parameters (e.g., solar radiation, boundary layer height, wind advection) (Li et al., 2020; Sinha et al., 2024).

The Spearman rank correlation coefficient (with a statistical significance level of $p = 0.05$) was also used to assess the statistical association between UPII for each pollutant under investigation and UHII. The analysis is conducted both over the entire study period (2019–2023) and for selected meteorologically significant events, also co-occurring, which are identified and characterized in the subsequent subsections. This dual approach (together with the lag-correlation analysis) enables a comprehensive assessment of both long-term monotonic relations and event-specific interactions between urban thermal and pollution anomalies.

3.2.2. Multiple linear regression

The multiple linear regression is employed to assess the relationship between meteorological variables and UPII, in order to quantify the relative contribution of each variable and identify which factors, among those considered, most strongly influence the correlation between UPII and UHII. Multiple linear regression provides a framework for assessing the contribution of each predictor to the variability of the response variable while controlling for the influence of the others. When predictors are standardized, this approach is particularly effective, as it enables a direct and comparable evaluation of their relative importance. It is widely used in the literature to disentangle meteorological influences on in-situ air pollution and surface thermal anomalies (Carslaw and Beevers, 2013; Grange and Carslaw, 2019). While more complex non-linear or machine-learning models could be used for predictive purposes, they do not offer the same interpretability regarding individual predictors, which is essential here for identifying the meteorological drivers that most strongly modulate the UHII-UPII relationship.

Here, the time series of daily UPII over the period 2019–2023, computed separately for each pollutant under investigation, is considered as the dependent variable, while the independent variables include a comprehensive set of daily meteorological parameters provided by the surface meteorological stations described in Sect. 2.3. The predictors investigated in the model are the meteorological parameters collected by the stations used in this study, including: daily average (T_{ave}), minimum (T_{min}), and maximum (T_{max}) air temperatures, daily temperature span ($E = T_{max} - T_{min}$), daily median (RH_{med}), minimum (RH_{min}), and maximum (RH_{max}) relative humidity, daily average (WS_{ave}), minimum (WS_{min}), and maximum (WS_{max}) wind speed.

Prior to defining the linear regression model, the potential severity of multicollinearity is assessed by applying the Variance Inflation Factor (VIF) for each predictor. The VIF quantifies the extent to which the variance of an estimated regression coefficient is inflated due to linear dependence among predictors. Formally, it is defined as:

$$VIF = \frac{1}{1 - R_i^2} \tag{4}$$

where R_i^2 denotes the coefficient of determination obtained by regressing the i-th predictor x_i against all other predictors in the model. In the absence of multicollinearity ($R_i^2 = 0$), $VIF = 1$, indicating no inflation of the coefficient variance. As the linear dependence among predictors increases, R_i^2 rises, resulting in higher VIF values and denoting more severe multicollinearity. Consistent with previous studies, predictors with VIF > 10 are considered indicative of problematic multicollinearity and are excluded from the model (Gómez et al., 2021; Cheng et al., 2022).

The analysis revealed that the parameters T_{min}, T_{max}, and E exhibit VIF values greater than 10 and were consequently excluded from the multiple linear regression.

Therefore, the regression model for a single pollutant is defined as follows:

$$UPII = \beta_0 + \beta_1 T_{ave} + \beta_2 RH_{med} + \beta_3 RH_{min} + \beta_4 RH_{max} + \beta_5 WS_{ave} + \beta_6 WS_{min} + \beta_7 WS_{max} + \epsilon \tag{5}$$

where β_0 is the intercept, $\beta_1 \ldots \beta_7$ are the regression coefficients associated with each predictor, and ϵ is the residual error term. All variables were standardized relative to their mean values (mean value equal to 0 and standard deviation equal to 1) prior to regression analysis. This standardization enabled direct comparison of the magnitudes of the regression coefficients, facilitating interpretation of predictors with differing physical units, such as air temperature, relative humidity, and wind speed. The final dataset consists of 2037 valid daily observations, corresponding to days for which complete data were available for all variables, including temperature, relative humidity, wind speed, and pollutant concentrations across both urban and rural stations. These observations were randomly divided into a training set (80 %) and a test set (20 %). Regression coefficients are estimated exclusively using the training set, while the test set is reserved for evaluating the predictive performance of the model.

To evaluate model performance and predictive accuracy, two statistical indicators are calculated: the adjusted coefficient of determination (R^2 adjusted) and the Root Mean Square Error (RMSE). The former provides a measure of the proportion of variance explained by the model while accounting for the number of predictors included (Gupta and Christopher, 2009). The latter quantifies the model prediction error by expressing the average deviation between observed and predicted values in the same units as the dependent variable, offering a direct measure of prediction accuracy (Cheng et al., 2013). For each target parameter and each predictor, the statistical significance of the corresponding regression coefficients is evaluated, assuming a statistical significance level of $p = 0.05$.

3.2.3. Identification of specific weather events

Based on the results of the multiple linear regression, further analysis was conducted to assess the influence of local and synoptic-scale meteorological conditions on the correlation between UPII and UHII. Specific days from the 2019–2023 study period were identified, each corresponding to one of four distinct meteorological patterns, determined for their potential to modulate atmospheric dispersion and thermal deviations from rural conditions. The selection was carried out using the following objective criteria:

1) Atmospheric stagnation events: periods during which the daily average wind speed is less than or equal to 2 m/s in at least 50 % of the considered meteorological stations (i.e., at least 5 out of 10 stations), persisting for a minimum of five consecutive days. This condition reflects large-scale stagnation patterns unfavourable to pollutant dispersion in the region (Palmieri et al., 2008).
2) Calm wind days: days during which the daily mean wind speed is below 1 m/s for at least twelve hours, in at least 50 % of the stations. These days are characterized by extremely weak ventilation and the potential accumulation of heat and air pollutants in the urban canopy layer (Vardoulakis et al., 2003).
3) Cold-air pooling nights: occur under meteorological conditions that promote significant nocturnal cooling, particularly in areas susceptible to cold-air pooling due to orographic features, such as river valleys. These conditions are typically characterized by clear skies and calm or nearly calm winds during nighttime. To identify days exhibiting such conditions, daily minimum temperatures recorded at the ML-13 urban meteorological station (see Table 2 for details) were compared with those measured at a station located in the Aniene River valley, east of Rome, in the locality of Tivoli Terme (RM-44, see Table 2 for details and Fig. 1 for the location of the station). The topography of this area favours the accumulation of cold air, often leading to lower minimum temperatures compared to those recorded

Table 2

List, geographical coordinates and altitude of meteorological monitoring stations considered in the present study. Station ML-44 is used only for the identification of cold-pooling nights.

Station ID	Lat. (° N)	Lon. (° E)	Elevation (m a.s.l.)
LA-01	41.83	12.54	83
LA-05	41.84	12.42	60
LA-06	41.95	12.46	45
ML-01	41.83	12.48	24
ML-08	41.90	12.44	55
ML-10	41.92	12.37	95
ML-11	41.96	12.40	135
ML-12	41.93	12.51	65
ML-13	41.93	12.53	42
ML-17	41.89	12.54	60
ML-44	41.95	12.73	78

even in the surrounding rural regions. By analysing the distribution of daily minimum temperature differences between the two stations across the entire study period, and considering only nights when the mean wind speed at both stations was below 1 m/s, according to the criteria chosen to also identify the calm wind conditions, it was possible to isolate, for each season, specific regions within the distribution characterized by larger temperature differences and slightly higher occurrence frequencies. During the summer season, the typical signature was less distinct within the temperature difference distribution, likely because of the increased frequency of favourable meteorological conditions (i.e., clear skies and calm winds), which reduces the contrast between pooling and not-pooling nights. Furthermore, the shorter duration of nighttime in summer limits radiative cooling, thereby reducing the amplitude of minimum temperature differences. Consequently, a seasonally variable threshold for temperature difference was adopted, with lower thresholds applied during summer. Cold-air pooling nights were ultimately defined using a fixed criterion for nighttime mean wind speed ($<$ 1 m/s at both stations) and season-specific threshold for the temperature difference between the two sites.

4) Heatwave episodes: periods during which the daily average air temperature exceeds the 90th percentile of the reference climatological distribution for, at least, four consecutive days. The reference period adopted is 1991–2020, using observations from the historical meteorological observatory of Collegio Romano, previously employed in climatological analyses of Rome (Di Bernardino et al., 2022). This criterion reflects the approach commonly used to define heatwaves in urban climate research (e.g., Zittis et al., 2022; Di Bernardino et al., 2023).

By isolating these peculiar meteorological conditions, the study aims to explore how atmospheric conditions 1–4 may influence the coupling between thermal and air pollution anomalies in the region.

In addition to analysing each meteorological event individually, co-occurring events were also considered to investigate their combined influence on the UHII-UPII relationship. Only combinations with a sufficient number of occurrences (i.e., more than 100 days over the 2019–2023 period) were included, ensuring statistical representativeness. This approach allows for assessing how overlapping meteorological conditions, such as simultaneous stagnation and calm wind or heatwave and calm wind, modulate the correlation between urban thermal and pollution anomalies.

4. Results

The results of this study are presented in accordance with the specific objectives outlined in Sect. 1, following the procedure detailed in Fig. 2. First, the spatial-temporal variability of UHII and UPII is explored, providing an overview of their magnitudes, seasonal patterns, and pollutant-specific differences, along with a lag-correlation analysis to identify potential temporal offsets between the two phenomena (Sect. 4.1). Then, the influence of meteorological variables on UPII is investigated through multiple linear regression analysis, identifying the factors that most significantly modulate the UHII–UPII relationship (Sect. 4.2). Finally, the correlations between UHII and UPII over the whole period under investigation and during selected meteorologically significant events are examined to highlight how extreme or specific weather conditions, also co-occurring, affect their coupling (Sect. 4.3).

4.1. Spatial-temporal variability of UHII and UPII

In Fig. 3, the time series of daily UHII and UPII computed for Rome over the period 2019–2023 are presented. The key statistics for the UHII and UPII time series are shown in Fig. 4 and summarized in Table S1. As detailed in Sect. 3.2, UHII values were computed as averages over the night-time period (22:00–06:00 CET), while UPII values were averaged over 24-h.

Fig. 4 and values in Table S1 clearly indicate that the greatest urban-rural variability is observed for NO_2, with a mean UPII of 27.3 μg/m^3, followed by NO and O_3, with mean values of 18.8 μg/m^3 and − 16.6 μg/m^3, respectively. However, both NO and O_3 exhibit substantial variability, with standard deviations of 20.2 μg/m^3 and 14.1 μg/m^3, respectively. In contrast, particulate matter shows smaller deviations from the concentrations measured in the rural area, with mean UPII values of 5.6 μg/m^3 for PM_{10} and 2.3 μg/m^3 for $PM_{2.5}$. Moreover, it is noteworthy that, for UHII and UPII for NO_2 and O_3, the mean and median values are very similar, whereas larger discrepancies between mean and median are observed for the UPII of particulate matters and NO, indicating higher spread in the dataset.

Fig. 3a shows that UHII exhibits a marked seasonal variability, assuming maxima during summer and minima during winter, in accordance with previous works (Ulpiani, 2021). Monthly averages are always positive and oscillate around 2.0 °C (average value over the period 2019–2023), with peaks frequently exceeding 3.0 °C in the warm season. On the contrary, the UHII values show higher variability, with maxima of 5.0 °C and minima that become negative, typically in wintertime, reaching −2.5 °C. This pattern reflects the enhanced heat accumulation in the urban environment during the summer, when the increased intensity of solar radiation favours heat accumulation in construction materials, such as asphalt and concrete. Being characterized by high thermal inertia and albedo, these materials efficiently absorb solar energy during the day and release it gradually at night, contributing to sustained elevated urban temperatures. In contrast, during the winter months, solar radiation is significantly weaker and nights are longer than in summer, limiting heat storage in urban surfaces and reducing the temperature difference between urban and rural areas (Voogt and Oke, 2003). Negative UHII values observed in winter can also result from transient meteorological phenomena, such as cold-air drainage, which may favour lower nocturnal temperatures in urban sites compared to surrounding rural areas. Additionally, differences in land cover and vegetation between urban and rural stations, as well as the presence of local radiative effects (e.g., stronger nocturnal cooling in open rural fields under clear-sky conditions), may further contribute to negative UHII values. Figs. 3b-3g depict the UPII time series for PM_{10}, $PM_{2.5}$, NO_2, NO, NO_2/NO, and O_3. For particulate matter, UPII shows a clear seasonal modulation, more marked for PM_{10} (panel b) than for $PM_{2.5}$ (panel c). The UPII for PM_{10} and $PM_{2.5}$ exhibit maxima in winter and minima in summer. For PM_{10}, the monthly averages become slightly negative in the summers of 2021 and 2022, while for $PM_{2.5}$, the monthly average oscillates between −2.0 μg/m^3 and 10.0 μg/m^3, with limited but non-negligible seasonal fluctuations. For nitrogen oxides (panels d and e), UPII assumes summer minima and winter maxima. In particular, UPII shows greater seasonal variability for NO than NO_2, the former being more directly influenced by local emissions, with average monthly peaks in winter slightly lower than 80.0 μg/m^3. As a consequence, monthly averages of UPII for NO_2/NO (panel f) oscillate between −8.0

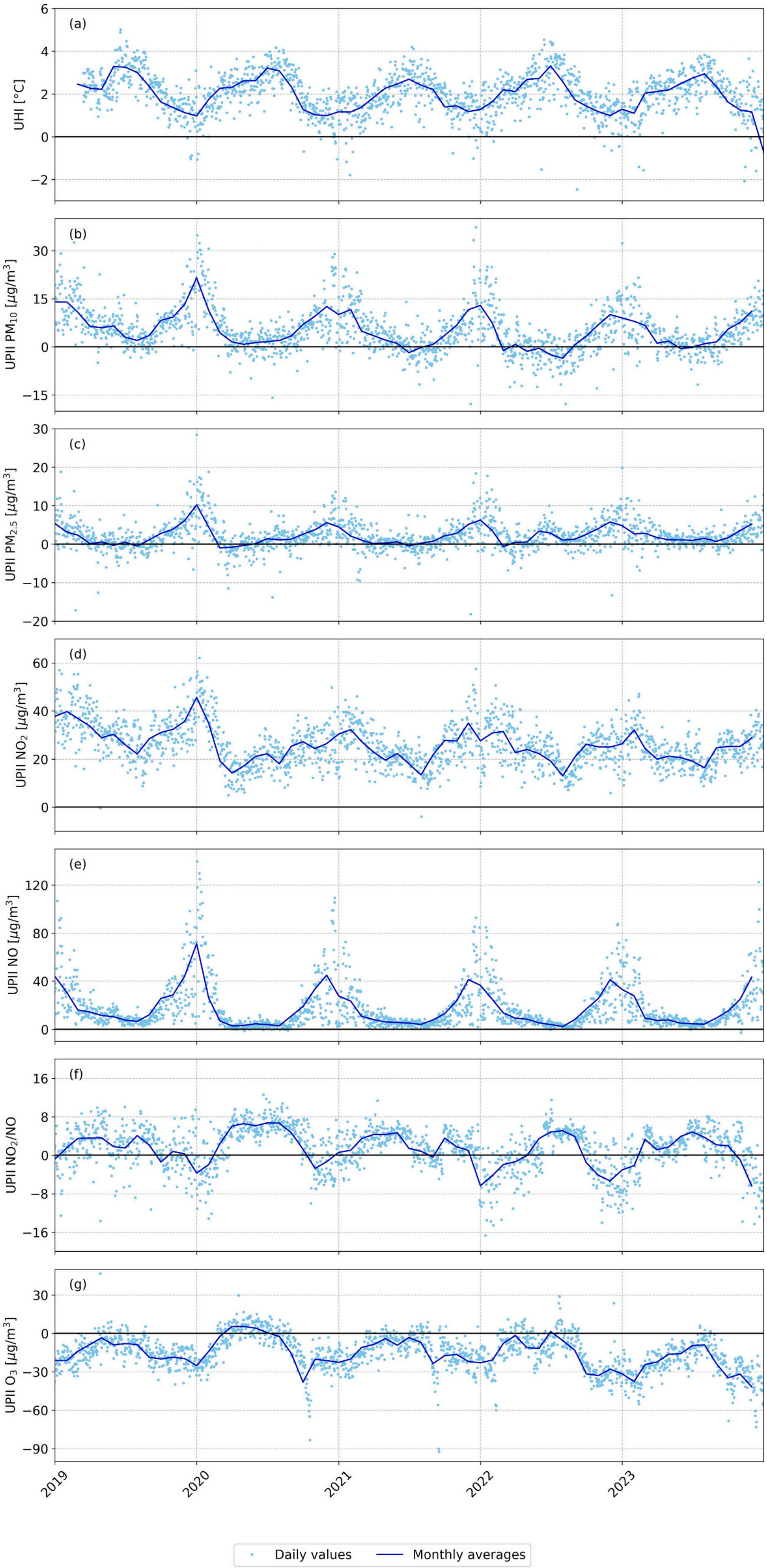

Fig. 3. Time series of (a) UHII and UPII for (b) PM$_{10}$, (c) PM$_{2.5}$, (d) NO$_2$, (e) NO, (f) NO$_2$/NO, and (g) O$_3$. Blue lines show the monthly average values, while cyan circles depict daily values. (For interpretation of the references to colour in this figure legend, the reader is referred to the web version of this article.)

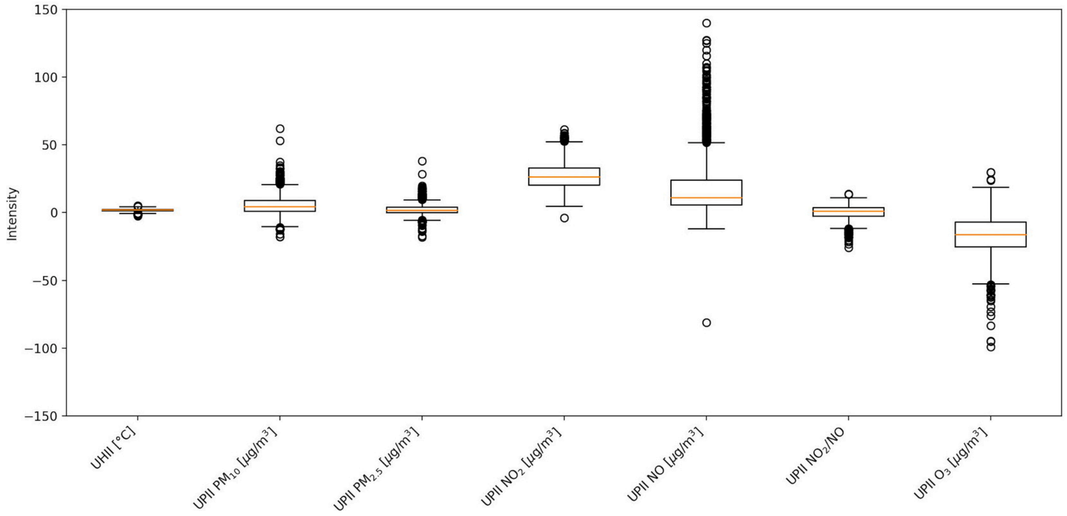

Fig. 4. Boxplot of UHII and UPII. Note that statistics for UPII are calculated as 24-h daily averages, while for UHII time series refer to the 22:00–06:00 CET time window.

and 8.0, generally assuming negative values in autumn-winter and positive values in spring-summer, in agreement with the enhanced photochemistry under the higher solar radiation and temperature conditions typical of the summer season. Interestingly, the UPII for O_3 (panel g) shows a strong negative intensity, particularly during the cold months, with values often below -30.0 µg/m^3. This inverse pattern can be attributed to the different underlying processes governing each atmospheric pollutant. While particulate matter and nitrogen oxides are primarily influenced by local emissions and ventilation conditions, O_3 formation and the NO_2/NO ratio are strongly affected by photochemical reactions. During summer, enhanced solar radiation and higher temperatures promote ozone production and photochemical aging, resulting in UPII patterns that follow UHII, whereas pollutants directly linked to emissions show an inverse seasonal trend with winter maxima and summer minima.

To further explore the relationship between spatial thermal and pollution differences, the co-variability between UHII and UPII is analysed by grouping UPII values into UHII intervals separately for each season, as presented in Fig. 5. The months are grouped according to the meteorological seasons as follows: winter (December, January, February), spring (March, April, May), summer (June, July, August), and autumn (September, October, November).

During winter (Fig. 5a), a general decreasing association between UHII and UPII for NO, O_3, PM_{10}, and $PM_{2.5}$ is observed. Conversely, NO_2 and NO_2/NO appear not to be related with variations in UHII. On the contrary, in summer (Fig. 5c), the relationship between UHII and UPII is much weaker and often flatter, especially for PM_{10} and $PM_{2.5}$. Spring and autumn (Fig. 5b and d, respectively) show an intermediate behaviour compared to the other seasons, with spring tending towards the summer pattern and autumn towards the winter pattern.

The stacked bar charts in Fig. 6 present the distribution of the number of days (y-axis) classified by UHII and UPII levels, across seasons

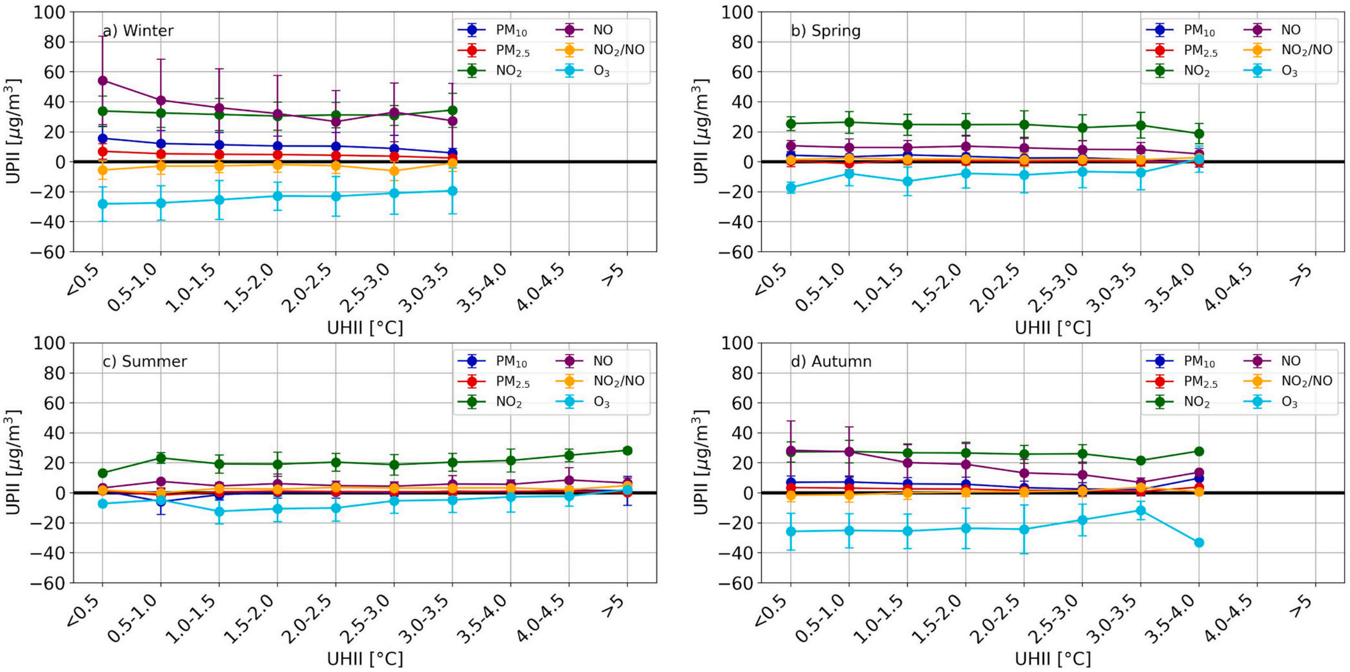

Fig. 5. Seasonal co-variability between UHII and UPII.

Fig. 6. Seasonal and annual distribution of the number of days (y-axis) classified by the UHII and UPII levels. The thresholds between Low, Medium, and High correspond to the 25th and 75th percentiles (Table S1).

and for the different air pollutants. For both UPII and UHII, the Low, Medium, and High categories were determined based on the data's statistical distribution. Specifically, the threshold between Low and Medium corresponds to the 25th percentile, while the threshold between Medium and High corresponds to the 75th percentile (see values in Table S1) of the statistical distribution of each dataset.

The data show a marked seasonal trend: in summer, a clear increase in the number of days with high UHII levels associated with medium and high UPII levels is observed, particularly for both particulate matter fractions and nitrogen oxides. This indicates that during the warm periods, the concentration of air pollutants becomes particularly high, especially in the urban area, where there is an intense heat accumulation. Despite the limited number of monitoring stations, the observed summertime coupling between UHII and UPII appears robust. Alternative definitions of the Low, Medium, and High bins could slightly redistribute the data; however, the overall seasonal patterns and the stronger summer association remain consistent. During the other seasons, the variation in the UPII levels across UHII classes is less pronounced, indicating a reduced influence of urban heating on pollution variation. The annual distribution of the UHII and UPII values reveals that most of the days fall in the medium and high UHII levels class, with a large share corresponding to the medium and high UPII levels. This suggests a persistent association between pollution inequality and UHII throughout the year, as discussed below.

Fig. S1 shows the full lag–correlation results computed over a ± 30-day window for UHII and the various UPII components. The correlations remain relatively stable across the lag range, with no substantial shifts in magnitude or sign for any variable. The only notable feature is the enhancement in absolute correlation for all analysed pollutants when the UHII time series is shifted backward by one day relative to the UPII (lag $= -1$). Beyond this point, the curves show no meaningful temporal structure. From a physical perspective, this behaviour is explained by the nature of the UHII metric itself, which, in this study, is computed as the average urban-rural temperature difference during the night-time hours. As such, each UHII value reflects thermal conditions influenced by atmospheric and surface processes occurring over the preceding daytime period, including pollutant emissions from traffic, heating, and chemical reactions. These emissions contribute to the modification of surface thermal properties and radiative balances which, in turn, affect the magnitude of nocturnal heat retention and the resulting UHII. Therefore, in what follows, the analyses regarding the correlation between UHII and UPII are performed by shifting the UHII time series back by one day with respect to UPII.

4.2. Multiple linear regression analysis

The results of the multiple linear regression are summarized in Table 3. The regression results indicate that daily average air temperature and daily average wind speed emerge as the primary drivers of UPII, while relative humidity plays a secondary, yet significant, role. Specifically, daily average temperature positively affects all pollutants, with the strongest influence for NO and NO_2, reflecting the robust sensitivity of nitrogen oxides to thermal conditions in the urban environment. Interestingly, O_3 also responds positively to temperature, despite a negative baseline, indicating enhanced photochemical formation under warmer conditions. Relative humidity has moderate effects, mainly through daily averages, while median, minimum, and maximum values contribute less consistently. Wind speed effects vary among pollutants, with daily averages showing the largest influence, particularly for PM_{10} and O_3, emphasizing the role of ventilation in controlling aerosol concentrations and ozone formation. The adjusted R^2 values range from 0.24 to 0.49, demonstrating that the model captures a substantial portion of the variability in UPII, while also highlighting the inherent complexity of pollutant dynamics and the influence of additional, unaccounted-for factors. The pollutant-specific sensitivities revealed by the regression underscore the peculiar response exhibited by air pollutants to specific meteorological drivers: particulate matter is strongly affected by wind-driven dispersion, nitrogen oxides are primarily temperature-sensitive, and ozone formation is modulated by both temperature and wind, reflecting photochemical processes and advection. Overall, the results highlight the pollutant-specific sensitivities of urban air pollution to meteorological conditions and establish a foundation for interpreting the subsequent analysis of UHII-UPII correlations.

4.3. Analysis of UHII-UPII correlations for the entire period under investigation and selected meteorological conditions

Fig. 7 shows the Spearman rank correlation coefficients between UHII and UPII for the entire period under investigation (2019–2023) and for selected meteorological events.

Considering the whole period under investigation, significant negative correlations are observed between UHII and UPII for NO ($\rho = -0.60$), PM_{10} ($\rho = -0.45$), and NO_2 ($\rho = -0.35$), indicating that stronger UHI events are typically associated with lower pollutant load in urban areas relative to rural counterparts. In contrast, UPII shows a significant, positive correlation for O_3 ($\rho = 0.54$), consistent with enhanced ozone formation in warmer urban areas under stable conditions. Also, NO_2/NO, which, as discussed previously, may be interpreted as a proxy for the age of the air mass with higher values connected with photochemically aged air masses, assumes a positive correlation coefficient ($\rho = 0.42$), suggesting older, more photochemically processed air during high UHII conditions. The strength of these correlations tends to increase under specific atmospheric patterns, linked to particular thermal and ventilation conditions. During calm wind days and atmospheric stagnation events, the absolute values of correlation coefficients are generally stronger, particularly for NO ($\rho = -0.71$ and -0.63, respectively) and O_3 ($\rho = 0.62$ and 0.59, respectively). These results suggest that reduced dispersion conditions, attributable to low ventilation and consequent atmospheric stability typically experienced during wintertime, enhance the coupling between urban thermal and pollution dynamics. Also, heatwave episodes determine an increase in the absolute value of the correlations for the different pollutants. Specifically, the strongest associations are again observed with O_3 ($\rho = 0.49$) and NO ($\rho = -0.66$), highlighting the combined effect of elevated temperatures and solar radiation on photochemical reactions and secondary pollutant formation. Interestingly, NO_2 correlations lose statistical significance during heatwaves, suggesting complex interactions between emissions, chemical processing, and meteorology. Cold-air pooling nights present a contrasting behaviour. Correlations are generally weaker, reflecting the more complex stratification and decoupling between surface heating and pollutant trapping in these conditions. Yet, even under cold-air pooling, NO ($\rho = -0.42$) and O_3 ($\rho = 0.56$) maintain the strongest associations, indicating persistent pollutant-specific sensitivities.

Fig. 8 shows the Spearman rank correlations between UHII and UPII for various combinations of co-occurring meteorological events. The results confirm the pollutant-specific sensitivity of the UHII-UPII coupling during compound events. Strong negative correlations are generally observed for NO and PM_{10}, particularly during co-occurrence of atmospheric stagnation and calm wind conditions ($\rho = -0.73$ for NO, $\rho = -0.56$ for PM_{10}) and heatwaves and calm wind conditions ($\rho = -0.73$ for NO, $\rho = -0.63$ for PM_{10}), indicating that stable, low-dispersion scenarios reduce urban-rural pollutant differences. $PM_{2.5}$ and NO_2 show moderate negative correlations, while O_3 and NO_2/NO consistently exhibit positive correlations, reflecting enhanced photochemical activity and aged air masses during high UHII events. Correlation strengths generally decrease when cold-air polling nights are included, highlighting the complex influence of stratification and vertical mixing.

Overall, this analysis demonstrates that the UHII-UPII relationship is strongly pollutant-dependent and sensitive to meteorological context, with compound events amplifying or weakening pollutant-specific responses.

The combined evaluation of the entire period and selected events allows for a comprehensive understanding of how urban heat modulates air pollution dynamics under both typical and extreme conditions, also in the case of compound events.

5. Discussion

Rome represents a characteristic Mediterranean urban environment, where a dense historical city core coexists with sprawling suburban districts and peri-urban green areas. This heterogeneous urban morphology, combined with complex local anemological conditions and with its position in the middle of the Mediterranean basin, makes the city an ideal case study for exploring the association between UPI and UHI.

Several studies have confirmed that Rome is significantly affected by both the UHI and UPI. As for the UHI, research spanning historical periods reports comparable magnitudes. For example, Colacino and Lavagnini (1982) reported UHII values ranging between 2.5 °C and 4.3 °C,

Table 3
Coefficients of the multiple linear regression for UPII of the various pollutants, together with the R^2 adjusted and RMSE values. The coefficients $\beta_0 \ldots \beta_7$ are determined following Eq. 5. For each target, the coefficients in bold indicate the statistically significant values. Statistical significance is marked as follows: *(p-value <0.05), ** (p-value <0.01), and *** (p-value <0.001).

	β_0 [°C]	β_1 [−]	β_2 [°C/%]	β_3 [°C/%]	β_4 [°C/%]	β_5 [°C/(m/s)]	β_6 [°C/(m/s)]	β_7 [°C/(m/s)]	R^2 adjusted	RMSE
UPII PM_{10}	**5.30*****	**3.41*****	**1.73*****	**0.54***	**0.54****	**1.90*****	0.01	0.18	0.40	5.81
UPII $PM_{2.5}$	**2.25*****	**1.16*****	**0.29****	0.01	0.01	**1.03*****	0.13	0.04	0.24	3.48
UPII NO_2	**26.35*****	**4.41*****	0.50	**1.64*****	0.51	**3.45*****	0.02	0.17	0.27	8.02
UPII NO	**18.15*****	**9.99*****	**2.79****	**2.38*****	0.46	**8.05*****	0.29	**1.04****	0.49	14.90
UPII NO_2/NO	**1.21*****	**1.31*****	**0.65****	**0.52*****	**0.45*****	**1.65*****	**0.16***	**0.39*****	0.36	3.61
UPII O_3	−15.67	**5.10*****	1.15	**0.95***	**2.09*****	**5.04*****	**0.54***	**0.71****	0.25	11.54

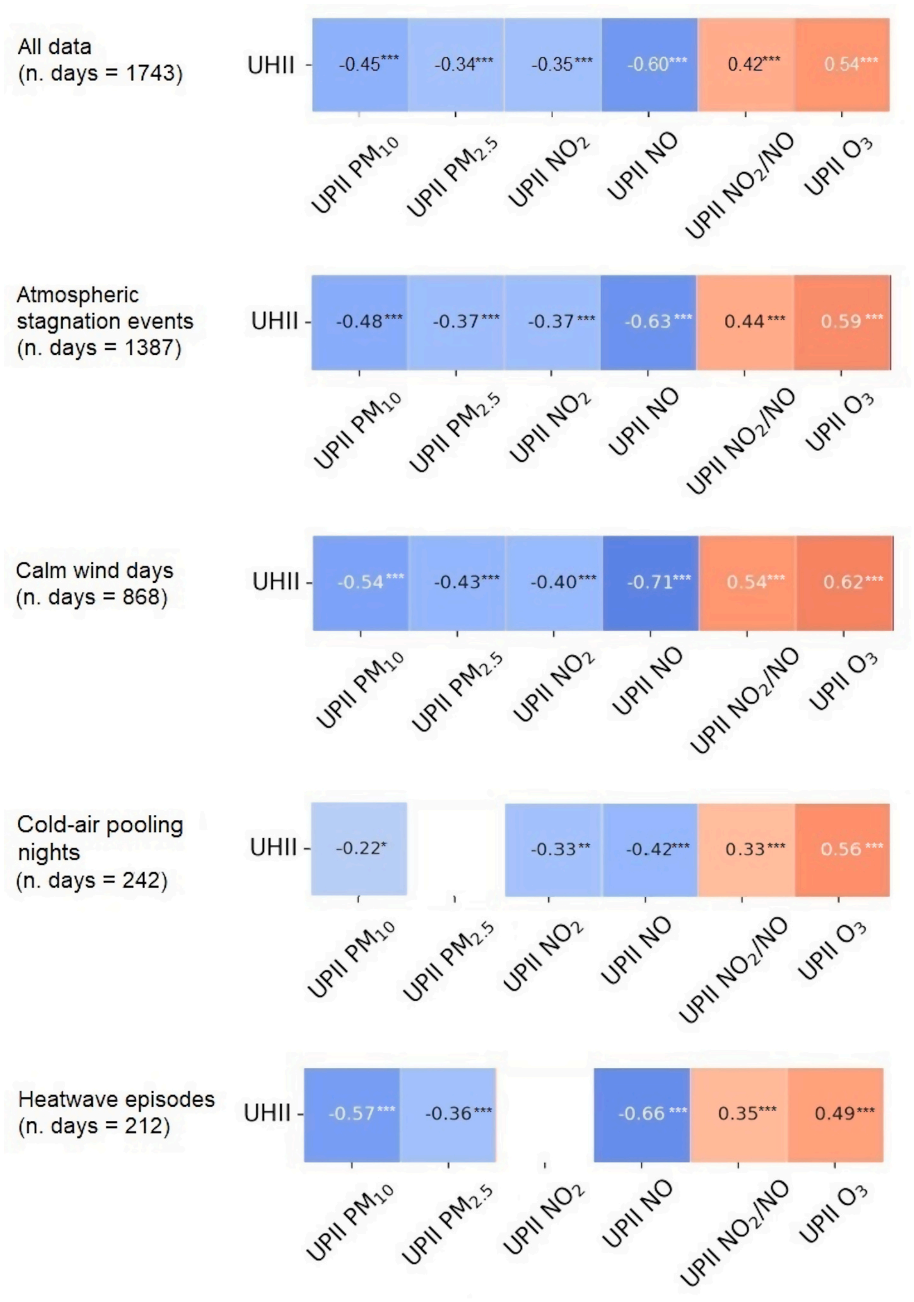

Fig. 7. Spearman rank correlation coefficients between UHII and UPII for the entire period under investigation (2019–2023) and for selected meteorological events. Darker colours denote stronger correlations, while lighter tones indicate weaker correlations. Squares with no annotation correspond to not statistically significant correlations (p-value$\geq$0.05). Statistical significance is marked as follows: *(p-value <0.05), ** (p-value <0.01), and *** (p-value <0.001). For each category, the number of days falling within that category is reported.

while Bonacquisti et al. (2006) simulated a maximum UHII of 5.0 °C, depending on seasonal variability, urban geometry, and surface thermal properties. More recently, Cecilia et al. (2023), assuming a linear relationship between measured air temperature and imperviousness, observed midnight UHII peaks of 3.4 °C. These findings are consistent with the present study, which reports a mean UHII of 2.0 °C (Table S1), with daily values ranging from −2.5 °C to 5.0 °C. The observed differences are primarily attributable to the temporal reference: while Cecilia et al. (2023) focused on 00:00, UHII here is calculated as the mean during the entire nocturnal period (22:00–06:00 CET), yielding a more integrated estimate (Fig. 3a).

Atmospheric pollution in Rome has reduced in recent years thanks to targeted environmental policies (Di Bernardino et al., 2022). Nevertheless, atmospheric pollutant concentrations remain notably higher in the urban centre compared to the rural areas, except for O_3, resulting in positive UPII for NO_2 (mean: 27.3 μg/m^3, standard deviation: 9.6 μg/m^3) and NO (mean: 18.8 μg/m^3, standard deviation: 9.6 μg/m^3) (Table S1). In line with Di Bernardino et al. (2025), UPII exhibits winter maxima and summer minima, particularly for PM_{10}, NO, and NO_2 (Fig. 3b–3g). In winter, increased vehicular traffic and domestic heating elevate emissions, especially in the urban areas, while atmospheric stability and reduced solar radiation inhibit vertical and horizontal pollutant dispersion. In contrast, rural areas show relatively constant pollutant levels throughout the year, reinforcing the urban–rural difference that defines UPII. Consequently, these seasonal differences arise from the combined effects of local emission patterns and

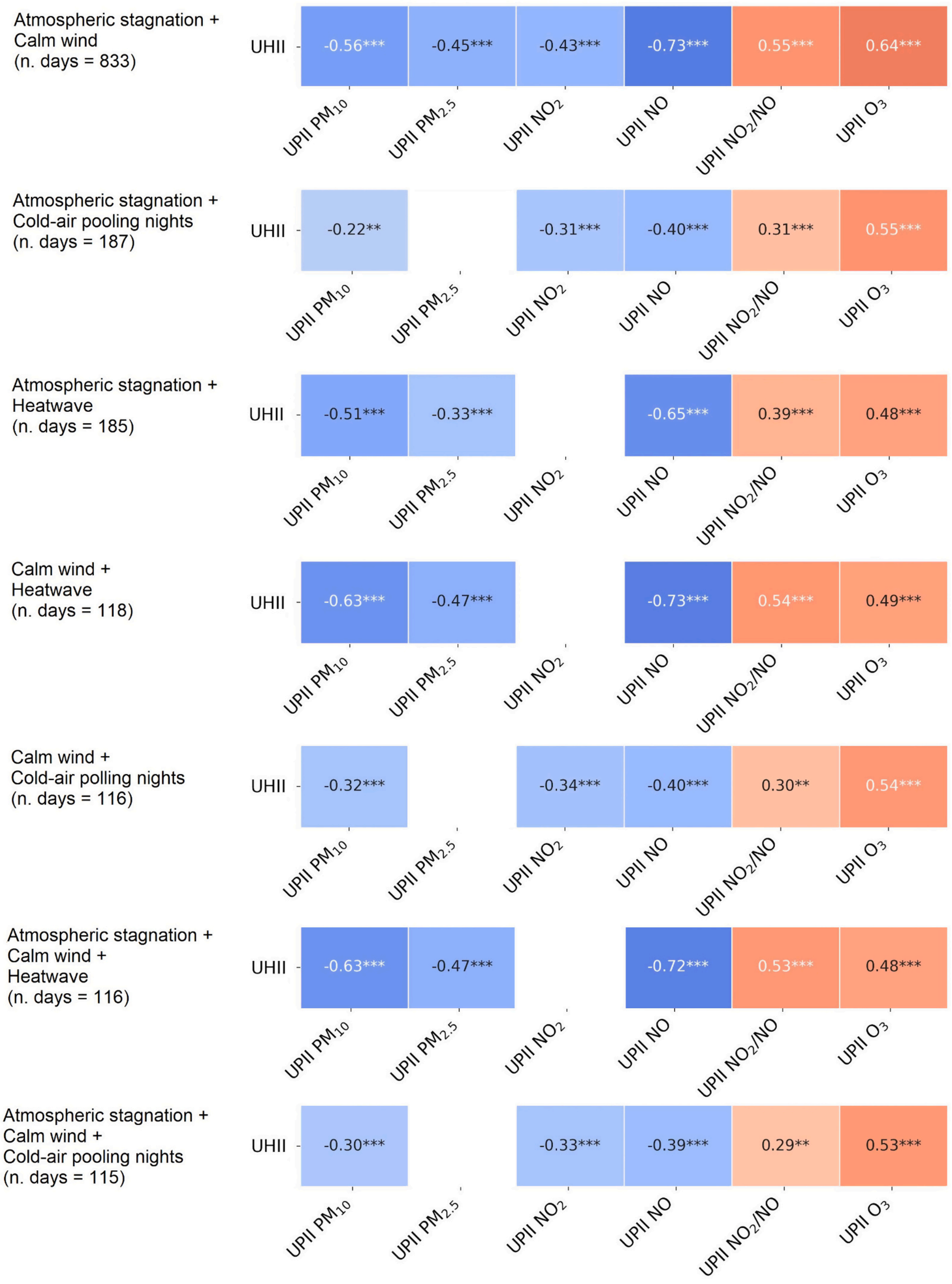

Fig. 8. Spearman rank correlation coefficients between UHII and UPII for combination of co-occurring selected meteorological events. Darker colours denote stronger correlations, while lighter tones indicate weaker correlations. Squares with no annotation correspond to not statistically significant correlations (p-value$\geq$0.05). Statistical significance is marked as follows: *(p-value <0.05), ** (p-value <0.01), and *** (p-value <0.001). For each category, the number of days falling within that category is reported.

peculiar meteorological conditions.

The seasonal co-variability analysis (Figs. 5 and 6) reveals a generally negative association between UHII and UPII for NO, PM_{10}, $PM_{2.5}$, and O_3 during winter. This suggests that higher UHII is often associated with reduced urban–rural pollutant contrasts, likely due to enhanced boundary layer development and pollutant dispersion during warmer urban nights. Conversely, in summer, this relationship becomes weaker, especially for aerosols, reflecting stronger photochemical activity and more efficient mixing, which diminishes the spatial pollutant difference. The UPII for O_3 remains predominantly negative across UHII intervals and seasons, except for the highest UHII values in spring and summer, supporting the role of NO titration in O_3 destruction reactions in high-emission urban cores.

Correlation analysis over the entire 2019–2023 period (Fig. 7) reveals strong negative associations between UHII and UPII for NO ($\rho = -0.60$), PM_{10} ($\rho = -0.45$), NO_2 ($\rho = -0.35$), and $PM_{2.5}$ ($\rho = -0.34$). In contrast, UHII is positively correlated with O_3 ($\rho = 0.54$) and NO_2/NO ($\rho = 0.42$), further indicating that the air mass is aged and that it is at a great distance from the emission sources. Also, the O_3 formation is enhanced by elevated solar radiation and, consequently, by higher atmospheric temperatures. Its concentrations tend to be higher in rural areas, where biogenic Volatile Organic Compounds (VOCs) are abundant and NO levels are relatively low, limiting the titration process that would otherwise degrade O_3, determining a positive correlation with UHII (Zhang et al., 2023; Guo et al., 2024). These results reflect the complex interplay between thermodynamic conditions, emission sources, and atmospheric chemistry. When the analysis is restricted to selected meteorological events, the strength of the UHII–UPII correlations becomes more pronounced. In particular, heatwave and calm wind conditions show the highest absolute correlation values, with negative correlations peaking for NO and positive correlations for O_3. The analysis of compound events reveals further amplification of these associations, in particular during days featuring co-occurring of heatwaves and calm winds or atmospheric stagnation (Fig. 8). This demonstrates that concurrent adverse weather events can intensify the coupling between urban heat and pollution anomalies, highlighting the importance of considering compound atmospheric conditions when assessing urban environmental risks.

Our findings are consistent with studies from other urban contexts. Hereher et al. (2022), using satellite-based products, reported maximum UHII values at Greater Cairo (Egypt) during winter, along with strong seasonal correlations with NO_2 ($R^2 = 0.59$ in spring) and CO ($R^2 = 0.51$ in winter). Similarly, Nasar-u-Minallah et al. (2025) identified significant positive correlations between UHII and both NO_2 and CO in Lahore (Pakistan). Li et al. (2020), employing observational data and WRF-Chem simulations in Berlin (Germany), observed UPII peaks during cold winter days and summer heatwaves, underlining the role of boundary layer dynamics and air temperature in promoting pollutant accumulation. Similar to this work, they identified a negative correlation between UHII and UPII for PM_{10}, particularly marked in summer. Li et al. (2018) further reported a nighttime UHII–UPII correlation of -0.31 for near-surface PM_{10}, attributing it to aerosol-induced longwave radiation trapping and reduced solar input. Wang et al. (2021), analysing the Yangtze River Delta (China), identified positive correlations between daytime UHII and O_3 and negative ones with PM_{10}, $PM_{2.5}$, NO_2, sulfur dioxide (SO_2), and carbon monoxide (CO). In India, Arunab and Mathew (2024) and Mathew and Arunab (2025) found moderate positive correlations between UHII and CO, NO_2, and O_3, while reporting weaker associations with formaldehyde, aerosols, and SO_2. In contrast, Mishra and Mathew (2022) found weak correlations between UHII and aerosol optical depth in Delhi (India), with R^2 ranging from 0.002 to 0.480.

Multiple linear regression analysis (Table 3) highlighted daily average air temperature and wind speed as the primary meteorological predictors of UPII, especially for NO ($\beta_1 = 9.99$ and $\beta_5 = 8.05\ ^\circ C/(m/s)$), O_3 ($\beta_1 = 5.10$ and $\beta_5 = 5.04\ ^\circ C/(m/s)$), and NO_2 ($\beta_1 = 4.41$ and $\beta_5 = 3.45\ ^\circ C/(m/s)$), while lower influence is found for the particulate matter fractions. These findings align with Lokoshchenko and Alekseeva (2023), who found that average daily wind speed and cloudiness were the dominant factors influencing UHII in Moscow (Russia), with multiple correlation coefficients of 0.82 and 0.76, respectively. Morris et al. (2001) reported similar dependencies in Melbourne (Australia), where nocturnal UHII scaled inversely with approximately the fourth root of wind speed and cloud cover. Finally, Rybarczyk et al. (2025) identified a strong positive association between $PM_{2.5}$ concentrations and air temperature in Quito (Ecuador), emphasizing the feedback between thermal conditions and aerosol amount. Patterns observed in Rome are consistent with other cities across climates, indicating that UHII–UPII dynamics share common mechanisms. On the other hand, this association is clearly modulated by meteorological conditions, particularly air temperature and wind speed, and further shaped by local factors, such as urban morphology and emission characteristics. These results have practical implications: urban planning measures can target periods of heightened heat and pollution stress (e.g., summer heatwaves, winter stagnation events) and inform environmental policies for mitigating combined heat and air pollution exposure.

Despite the robustness of the adopted methodology and the comprehensive multi-year dataset, several limitations of the present study must be acknowledged. First, the reliance on fixed urban and rural stations may not fully capture the spatial heterogeneity of urban environments or the influence of specific local sources. The geographical mismatch between this rural site and the location of the meteorological stations used for UHII calculations may introduce uncertainties, especially under heterogeneous emission and dispersion conditions. A more spatially resolved approach, integrating multiple rural and peri-urban reference sites, would reduce this potential bias and allow for a more robust characterization of urban–rural contrasts. Similarly, the temporal window analysed (2019–2023) limits the capacity to identify long-term trends and potential shifts induced by climate change or emission policy changes. Then, the UHII-UPII diurnal mismatch complicates direct comparison. In fact, UHII typically reaches its maximum intensity during nighttime hours, primarily due to the thermal inertia and high heat storage capacity of urban materials, which release accumulated heat after sunset. In contrast, UPII tends to peak during daytime, when anthropogenic emissions, particularly from vehicular traffic, residential heating, and industrial activities, are at their highest. Besides, the study focuses exclusively on atmospheric dynamics and thermodynamic conditions, without explicitly accounting for radiative feedback and photochemical processes, which are known to significantly modulate both pollutant concentrations (e.g., ozone formation) and the energy balance of urban areas. As such, the results primarily reflect the influence of meteorology-driven dispersion and accumulation mechanisms and may underestimate the role of chemical transformation and aerosol–radiation interactions. In addition, it is important to stress that statistical correlations presented in this study do not imply strict causation. Mechanistic interpretations, such as the role of daytime emissions trapped in the nocturnal boundary layer, are intended as physically consistent hypotheses aligned with established atmospheric processes, rather than direct inferences from the correlation analysis alone. Finally, this study relies on linear regression models to explore the statistical relationships between UPII and meteorological variables, with adjusted R^2 values ranging from 0.24 to 0.49 (see Table 3). This indicates that a substantial fraction of the variability in UPII, particularly for $PM_{2.5}$ and O_3, remains unexplained by the meteorological predictors included in the present analysis. Several factors may account for this. First, key atmospheric variables that modulate both pollutant concentrations and urban thermal dynamics, such as planetary boundary layer height, cloud cover, and incoming solar radiation, could not be incorporated because they are not routinely measured by the operational monitoring networks used in this study. These parameters strongly influence vertical mixing, photochemical activity, and dilution processes, and their absence inevitably limits the model's ability to capture day-to-day variability in UPII. Second, the coarse temporal resolution of particulate matter data (available only as daily averages from ARPA Lazio) may further smooth short-term variability and reduce the model's sensitivity. Additionally, secondary formation processes (particularly for O_3 and fine particles) are inherently non-linear and can respond to complex interactions between emissions, solar radiation, and chemical reactions that are not adequately represented by linear models. For these reasons, the regression results should be interpreted as first-order approximations of meteorological influence on UPII. More advanced approaches, such as non-linear regression, generalized additive models (GAMs), machine learning algorithms, or causal inference frameworks integrating statistical analysis with numerical simulations, could better capture the complex and potentially non-linear interactions between urban climate and air quality.

To address these limitations, future research should consider expanding the temporal coverage to include longer climatic periods, testing machine learning algorithms, and adopting more flexible or spatially resolved definitions of UHII and UPII. Integrating radiative and photochemical components into the analytical framework, possibly through coupled atmospheric chemistry and radiative transfer models, would allow for a more complete assessment of the feedback mechanisms between urban warming and air pollution. As demonstrated, cloud cover and incoming solar radiation play a fundamental role in the association between UPII and UHII. Incorporating radiative and photochemical processes would allow a more complete assessment of feedbacks between urban warming and air pollution, providing valuable insights for sustainable urban management.

6. Conclusions

This study presents a comprehensive analysis aimed at exploring the relationship between UHII and UPII over the city of Rome (Italy) over the period 2019–2023, using observations of air temperature, atmospheric particulate matter fractions (PM_{10} and $PM_{2.5}$) and gaseous pollutants (NO, NO_2, and O_3) concentrations, together with the NO_2/NO ratio. UHII-UPII interactions were examined through lag-correlation analysis, multiple linear regression, and Spearman rank correlations, including evaluations under specific meteorological conditions.

The key findings can be summarized as follows:

- UHII and UPII exhibit pronounced but opposite seasonal cycles for all pollutants except for O_3, with UHII peaking in summer and UPII in winter. This pattern reflects seasonal differences in anthropogenic emissions, boundary layer dynamics, and atmospheric stability;
- during summer, high UHII frequently coincides with medium-to-high UPII levels, especially for PM_{10}, $PM_{2.5}$, NO, and NO_2. This highlights the concurrent stress from heat and pollution under summer conditions;
- the lag-correlation analysis demonstrates that UHII is most strongly associated with UPII when it is shifted one day backward. This result is physically consistent, considering that UHII is calculated from nighttime temperatures, which reflect the atmospheric conditions influenced by pollutant emissions from the previous day. During stable nighttime conditions, these pollutants tend to remain trapped in the nocturnal boundary layer, enhancing UPII;
- air temperature and wind speed emerge as the dominant meteorological drivers of UHII-UPII variability, influencing both heat accumulation and pollutant dispersion;
- correlation analysis reveals generally negative relationships between UHII and UPII for PM_{10}, $PM_{2.5}$, NO_2, and NO, and positive correlations for the NO_2/NO ratio as well as for O_3, largely dictated by their opposing seasonal behaviours and by photochemical and titration mechanisms;
- calm wind conditions and heatwave events, also co-occurring, significantly amplify the UHII-UPII coupling, particularly for O_3, NO, and PM_{10}. This highlights the synergistic role of adverse weather conditions in enhancing both urban warming and pollution exposure risks.

Overall, the results show that UHII-UPII interactions arise from a combination of meteorological drivers, emission patterns, and chemical processes, and cannot be interpreted solely through thermal anomalies or pollutant loadings.

Beyond its scientific contribution, the proposed framework may also be used as a predictive tool to simulate future UHII and UPII scenarios under different climatic and land-use conditions, including increasing greenhouse gas emissions, when UHI effects may amplify climate change impacts. Such applications can support the design of mitigation and adaptation strategies, such as nature-based solutions, optimized ventilation corridors, or targeted emission reduction policies. Moreover, the framework offers socio-economic insights by highlighting implications for health risks, energy demand, and uneven exposure among urban populations, thus supporting the design of adaptation strategies that are both effective and equitable. More broadly, the results contribute to ongoing efforts aligned with Sustainable Development Goals 11 and 13 of the 2030 Agenda for Sustainable Development (Walsh et al., 2022).

CRediT authorship contribution statement

A. Di Bernardino: Writing – review & editing, Writing – original draft, Visualization, Validation, Supervision, Software, Resources, Project administration, Methodology, Investigation, Funding acquisition, Formal analysis, Data curation, Conceptualization. **S. Argentini:** Writing – review & editing, Methodology, Funding acquisition, Conceptualization. **E. Brattich:** Writing – review & editing, Supervision, Resources, Project administration, Methodology, Funding acquisition, Conceptualization. **M. Campanelli:** Writing – review & editing, Conceptualization. **G. Casasanta:** Writing – review & editing. **A. Cecilia:** Writing – review & editing, Visualization, Validation, Software, Resources, Methodology, Data curation. **M. Erriu:** Writing – review & editing, Software, Resources, Data curation. **S. Falasca:** Writing – review & editing, Conceptualization. **A. Faggi:** Writing – review & editing. **A.M. Siani:** Writing – review & editing, Methodology, Conceptualization.

Fundings

This study was supported by the PRIN 2022 “uRban hEat and pollution iSlands inTerAction in Rome and possible mitigation Strategies (RESTART)” project, funded by the Italian Ministry of University and Research (Prot. 2022KZ2AJE), CUP B53D23007210006. Stefania Argentini and Giampietro Casasanta acknowledge the LIFE21-GIE-EL-LIFE “A System for Integrated EnviRonmental Information in Urban areaS (SIRIUS)” project and the LIFE17 CCA/GR/000108 “implementation of a forecAsting System for urban heaT Island effect for the development of urban adaptation strategy (ASTI)” project.

Declaration of competing interest

The authors declare the following financial interests/personal relationships which may be considered as potential competing interests: (Annalisa Di Bernardino reports financial support was provided by Italian Ministry of University and Research. If there are other authors, they declare that they have no known competing financial interests or personal relationships that could have appeared to influence the work reported in this paper.)

Acknowledgments

The authors gratefully acknowledge ARPA Lazio for providing air quality data and Meteo Lazio and CNR-ISAC for providing weather data.

Appendix A. Supplementary data

Supplementary data to this article can be found online at https://doi.org/10.1016/j.atmosres.2025.108702.

Data availability

Data will be made available on request.

References

Arunab, K.S., Mathew, A., 2024. Quantifying urban heat island and pollutant nexus: a novel geospatial approach. Sustain. Cities Soc. 101, 105117. https://doi.org/10.1016/j.scs.2023.105117.

Bakaeva, N., Le, M.T., 2022. Determination of urban pollution islands by using remote sensing technology in Moscow, Russia. Ecol. Informatics 67, 101493. https://doi.org/10.1016/j.ecoinf.2021.101493.

Baklanov, A., Molina, L.T., Gauss, M., 2016. Megacities, air quality and climate. Atmos. Environ. 126, 235–249. https://doi.org/10.1016/j.atmosenv.2015.11.059.

Battista, G., de Lieto Vollaro, R., 2017. Correlation between air pollution and weather data in urban areas: Assessment of the city of Rome (Italy) as spatially and temporally independent regarding pollutants. Atmos. Environ. 165, 240–247. https://doi.org/10.1016/j.atmosenv.2017.06.050.

Beck, H.E., Zimmermann, N.E., McVicar, T.R., Vergopolan, N., Berg, A., Wood, E.F., 2018. Present and future Köppen-Geiger climate classification maps at 1-km resolution. Sci. Data 5 (1), 1–12. https://doi.org/10.1038/sdata.2018.214.

Bonacquisti, V., Casale, G.R., Palmieri, S., Siani, A.M., 2006. A canopy layer model and its application to Rome. Sci. Total Environ. 364 (1–3), 1–13. https://doi.org/10.1016/j.scitotenv.2005.09.097.

Cao, C., Lee, X., Liu, S., Schultz, N., Xiao, W., Zhang, M., Zhao, L., 2016. Urban heat islands in China enhanced by haze pollution. Nat. Commun. 7 (1), 12509. https://doi.org/10.1038/ncomms12509.

Carslaw, D.C., Beevers, S.D., 2013. Characterising and understanding emission sources using bivariate polar plots and k-means clustering. Environ. Model. Softw. 40, 325–329. https://doi.org/10.1016/j.envsoft.2012.09.005.

Cecilia, A., Casasanta, G., Petenko, I., Conidi, A., Argentini, S., 2023. Measuring the urban heat island of Rome through a dense weather station network and remote sensing imperviousness data. Urban Clim. 47, 101355. https://doi.org/10.1016/j.uclim.2022.101355.

Čeplová, N., Kalusová, V., Lososová, Z., 2017. Effects of settlement size, urban heat island and habitat type on urban plant biodiversity. Landsc. Urban Plan. 159, 15–22. https://doi.org/10.1016/j.landurbplan.2016.11.004.

Chapman, S., Watson, J.E., Salazar, A., Thatcher, M., McAlpine, C.A., 2017. The impact of urbanization and climate change on urban temperatures: a systematic review. Landsc. Ecol. 32 (10), 1921–1935. https://doi.org/10.1007/s10980-017-0561-4.

Cheng, Z., Jiang, J., Fajardo, O., Wang, S., Hao, J., 2013. Characteristics and health impacts of particulate matter pollution in China (2001−2011). Atmos. Environ. 65, 186–194. https://doi.org/10.1016/j.atmosenv.2012.10.022.

Cheng, J., Sun, J., Yao, K., Xu, M., Cao, Y., 2022. A variable selection method based on mutual information and variance inflation factor. Spectrochim. Acta A Mol. Biomol. Spectrosc. 268, 120652. https://doi.org/10.1016/j.saa.2021.120652.

Colacino, M., Lavagnini, A., 1982. Evidence of the urban heat island in Rome by climatological analyses. Arch. Meteorol. Geophys. Bioclimatol. Ser. B Theoret. Appl. Climatol. 31 (1–2), 87–97. https://doi.org/10.1007/BF02311344.

Copernicus, E.U., 2018. Copernicus Land Monitoring Service. Corine Land Cover data.

Crutzen, P.J., 2004. New directions: the growing urban heat and pollution" island" effect-impact on chemistry and climate. Atmos. Environ. 38 (21), 3539–3540.

Di Bernardino, A., Iannarelli, A.M., Casadio, S., Mevi, G., Campanelli, M., Casasanta, G., Cede, A., Tiefengraber, M., Siani, A.M., Spinei, E., Cacciani, M., 2021. On the effect of sea breeze regime on aerosols and gases properties in the urban area of Rome, Italy. Urban Clim. 37, 100842. https://doi.org/10.1016/j.uclim.2021.100842.

Di Bernardino, A., Iannarelli, A.M., Diémoz, H., Casadio, S., Cacciani, M., Siani, A.M., 2022. Analysis of two-decade meteorological and air quality trends in Rome (Italy). Theor. Appl. Climatol. 149 (1), 291–307. https://doi.org/10.1007/s00704-022-04047-y.

Di Bernardino, A., Falasca, S., Iannarelli, A.M., Casadio, S., Siani, A.M., 2023. Effect of heatwaves on urban sea breeze, heat island intensity, and outdoor thermo-hygrometric comfort in Rome (Italy). Urban Clim. 52, 101735. https://doi.org/10.1016/j.uclim.2023.101735.

Di Bernardino, A., Erriu, M., Falasca, S., Siani, A.M., 2025. Exploring different methods to evaluate the Urban Pollution Island Intensity based on multi-year observations of aerosol and gases. Atmos. Pollut. Res. 102677. https://doi.org/10.1016/j.apr.2025.102677.

Falasca, S., Di Bernardino, A., Salata, F., 2023. On the identification and characterization of outdoor thermo-hygrometric stress events. Urban Clim. 52, 101728. https://doi.org/10.1016/j.uclim.2023.101728.

Fallmann, J., Forkel, R., Emeis, S., 2016. Secondary effects of urban heat island mitigation measures on air quality. Atmos. Environ. 125, 199–211. https://doi.org/10.1016/j.atmosenv.2015.10.094.

Geletič, J., Lehnert, M., Savić, S., Milošević, D., 2019. Inter−/intra-zonal seasonal variability of the surface urban heat island based on local climate zones in three central European cities. Build. Environ. 156, 21–32. https://doi.org/10.1016/j.buildenv.2019.04.011.

Gobbi, G.P., Angelini, F., Barnaba, F., Costabile, F., Baldasano, J.M., Basart, S., Sozzi, R., Bolignano, A., 2013. Changes in particulate matter physical properties during Saharan advections over Rome (Italy): a four-year study, 2001–2004. Atmos. Chem. Phys. 13 (15), 7395–7404. https://doi.org/10.5194/acp-13-7395-2013.

Gómez, R.S., Sánchez, A.R., García, C.G., Pérez, J.G., 2021. The VIF and MSE in raise regression. Quantitative Meth. Econ. Fin. 325. https://doi.org/10.3390/math8040605.

Grange, S.K., Carslaw, D.C., 2019. Using meteorological normalisation to detect interventions in air quality time series. Sci. Total Environ. 653, 578–588. https://doi.org/10.1016/j.scitotenv.2018.10.344.

Guan, L., Yang, J., Bell, J.M., 2007. Cross-correlations between weather variables in Australia. Build. Environ. 42 (3), 1054–1070. https://doi.org/10.1016/j.buildenv.2006.01.010.

Guattari, C., Evangelisti, L., Balaras, C.A., 2018. On the assessment of urban heat island phenomenon and its effects on building energy performance: a case study of Rome (Italy). Energ. Buildings 158 (605–615), 20. https://doi.org/10.1016/j.enbuild.2017.10.050.

Guo, P., Su, Y., Sun, X., Liu, C., Cui, B., Xu, X., Ouyang, Z., Wang, X., 2024. Urban–rural comparisons of biogenic volatile organic compounds and ground-level ozone in Beijing. Forests 15 (3), 508. https://doi.org/10.3390/f15030508.

Gupta, P., Christopher, S.A., 2009. Particulate matter air quality assessment using integrated surface, satellite, and meteorological products: Multiple regression approach. J. Geophys. Res. Atmos. 114 (D14). https://doi.org/10.1029/2008JD011496.

Hauke, J., Kossowski, T., 2011. Comparison of values of Pearson's and Spearman's correlation coefficients on the same sets of data. Quaestiones geographicae 30 (2), 87–93.

Heaviside, C., Macintyre, H., Vardoulakis, S., 2017. The urban heat island: implications for health in a changing environment. Curr. Environ. Health Rep. 4, 296–305. https://doi.org/10.1007/s40572-017-0150-3.

Hereher, M., Eissa, R., Alqasemi, A., El Kenawy, A.M., 2022. Assessment of air pollution at Greater Cairo in relation to the spatial variability of surface urban heat island. Environ. Sci. Pollut. Res. 1-14. https://doi.org/10.1007/s11356-021-17383-9.

Jiang, S., Han, C., Ma, Y., Ji, J., Chen, G., Guo, Y., 2024. Temporal dynamic effects of meteorological factors and air quality on the physical health of the older adults in Shenzhen, China. Front. Public Health 12, 1289253. https://doi.org/10.3389/fpubh.2024.1289253.

Kikon, N., Singh, P., Singh, S.K., Vyas, A., 2016. Assessment of urban heat islands (UHI) of Noida City, India using multi-temporal satellite data. Sustain. Cities Soc. 22, 19–28. https://doi.org/10.1016/j.scs.2016.01.005.

Kong, G., Peng, J., Corcoran, J., 2025. Modelling urban heat island effects: a global analysis of 216 cities using machine learning techniques. Comput. Urban Sci. 5 (26), 1–12. https://doi.org/10.1007/s43762-025-00178-w.

Kousis, I., Pigliautile, I., Pisello, A.L., 2021. Intra-urban microclimate investigation in urban heat island through a novel mobile monitoring system. Sci. Rep. 11 (1), 9732. https://doi.org/10.1038/s41598-021-88344-y.

Li, H., Meier, F., Lee, X., Chakraborty, T., Liu, J., Schaap, M., Sodoudi, S., 2018. Interaction between urban heat island and urban pollution island during summer in Berlin. Sci. Total Environ. 636, 818–828. https://doi.org/10.1016/j.scitotenv.2018.04.254.

Li, H., Sodoudi, S., Liu, J., Tao, W., 2020. Temporal variation of urban aerosol pollution island and its relationship with urban heat island. Atmos. Res. 241, 104957. https://doi.org/10.1016/j.atmosres.2020.104957.

Lokoshchenko, M.A., Alekseeva, L.I., 2023. Influence of meteorological parameters on the urban heat island in Moscow. Atmosphere 14 (3), 507. https://doi.org/10.3390/atmos14030507.

Matak, L., Momen, M., 2025. Enhancing air pollution forecasts in cities by characterizing the urban heat island effects on planetary boundary layers. Atmos. Res. 315, 107923. https://doi.org/10.1016/j.atmosres.2025.107923.

Mathew, A., Arunab, K.S., 2025. Urban heat island and pollutant correlations in Bangalore, India using Geospatial Techniques. Solar Compass 100108. https://doi.org/10.1016/j.solcom.2025.100108.

Mishra, M.K., Mathew, A., 2022. Investigating the spatio-temporal correlation between urban heat island and atmospheric pollution island interaction over Delhi, India using geospatial techniques. Arab. J. Geosci. 15 (20), 1591. https://doi.org/10.1007/s12517-022-10854-4.

Morris, C.J.G., Simmonds, I., Plummer, N., 2001. Quantification of the influences of wind and cloud on the nocturnal urban heat island of a large city. J. Appl. Meteorol. 40 (2), 169–182. https://doi.org/10.1175/1520-0450(2001)040<0169:QOTIOW>2.0.CO;2.

Nasar-u-Minallah, M., Jabeen, M., Parveen, N., Abdullah, M., Nuskiya, M.H.F., 2025. Exploring the seasonal variability and nexus between urban air pollution and urban heat islands in Lahore, Pakistan. Acta Geophysica 1-21. https://doi.org/10.1007/s11600-025-01574-w.

Nastos, P., Saaroni, H., 2024. Living in Mediterranean cities in the context of climate change: a review. Int. J. Climatol. 44 (10), 3169–3190. https://doi.org/10.1002/joc.8546.

Oke, T.R., Mills, G., Christen, A., Voogt, J.A., 2017. Urban Climates. Cambridge University Press. https://doi.org/10.1017/9781139016476.

Palmieri, S., Durante, G., Siani, A.M., Casale, G.R., 2008. Atmospheric Stagnation Episodes and Hospital Admissions.

Perrino, C., Canepari, S., Catrambone, M., Dalla Torre, S., Rantica, E., Sargolini, T., 2009. Influence of natural events on the concentration and composition of atmospheric particulate matter. Atmos. Environ. 43 (31), 4766–4779. https://doi.org/10.1016/j.atmosenv.2008.06.035.

Petenko, I., Mastrantonio, G., Viola, A., Argentini, S., Coniglio, L., Monti, P., Leuzzi, G., 2011. Local circulation diurnal patterns and their relationship with large-scale flows in a coastal area of the Tyrrhenian Sea. Bound.-Layer Meteorol. 139, 353–366. https://doi.org/10.1007/s10546-010-9577-x.

Rowlinson, M.J., Carpenter, L.J., Evans, M.J., Lee, J.D., Andersen, S., Sherwen, T., Callaghan, A.B., Sommariva, R., Bloss, W., Hou, S., Crilley, L.R., Pfeilsticker, K., Weyland, B., Ryerson, T.B., Veres, P.R., Campuzano-Jost, P., Guo, H., Nault, B.A., Jimenez, J.L., Fomba, K.W., 2025. Observations of tropospheric HONO are incompatible with understanding of atmospheric chemistry. EGUsphere 2025, 1–32. https://doi.org/10.5194/egusphere-2025-830.

Roxon, J., Ulm, F.J., Pellenq, R.M., 2020. Urban heat island impact on state residential energy cost and CO2 emissions in the United States. Urban Clim. 31, 100546. https://doi.org/10.1016/j.uclim.2019.100546.

Rybarczyk, Y., Zalakeviciute, R., Ereminaite, M., Costa-Stolz, I., 2025. Causal effect of PM2. 5 on the urban heat island. Front. Big Data 8, 1546223. https://doi.org/10.3389/fdata.2025.1546223.

Sinha, S., Banerjee, A., Patnaik, A., Paul, S.K., 2024. Exploring the linkages between urban heat islands and urban pollution islands in tropical countries: a comprehensive review. Develop. Environ. Sci. 15, 529–554. https://doi.org/10.1016/B978-0-443-21948-1.00025-X.

Tremmel, H.G., Schlager, H., Konopka, P., Schulte, P., Arnold, F., Klemm, M., Droste-Franke, B., 1998. Observations and model calculations of jet aircraft exhaust products at cruise altitude and inferred initial OH emissions. J. Geophys. Res.-Atmos. 103, 10803–10816. https://doi.org/10.1029/97JD03451.

Tseng, K.H., Wang, J.L., Cheng, M.T., Tsuang, B.J., 2009. Assessing the relationship between air mass age and summer ozone episodes based on photochemical indices. Aerosol Air Qual. Res. 9 (2), 149–171. https://doi.org/10.4209/aaqr.2008.12.0062.

Ulpiani, G., 2021. On the linkage between urban heat island and urban pollution island: Three-decade literature review towards a conceptual framework. Sci. Total Environ. 751, 141727. https://doi.org/10.1016/j.scitotenv.2020.141727.

Vardoulakis, S., Fisher, B.E.A., Pericleous, K., Gonzalez-Flesca, N., 2003. Modelling air quality in street canyons: a review. Atmos. Environ. 37 (2), 155–182. https://doi.org/10.1016/S1352-2310(02)00857-9.

Voogt, J.A., Oke, T.R., 2003. Thermal remote sensing of urban climates. Remote Sens. Environ. 86 (3), 370–384. https://doi.org/10.1016/S0034-4257(03)00079-8.

Walsh, P.P., Banerjee, A., Murphy, E., 2022. The UN 2030 agenda for sustainable development. In: Partnerships and the Sustainable Development Goals. Springer International Publishing, Cham, pp. 1–12. https://doi.org/10.1007/978-3-031-07461-5_1.

Wang, Y., Guo, Z., Han, J., 2021. The relationship between urban heat island and air pollutants and them with influencing factors in the Yangtze River Delta, China. Ecol. Indic. 129, 107976. https://doi.org/10.1016/j.ecolind.2021.107976.

Wang, Q., Wang, T., Zhao, S., Yang, K., Wen, X., Zhao, M., Luo, F., Jiang, B., Jin, Y., Zhang, B., 2023. Comprehensive meteorological factors analysis and lag correlation study for cyanobacterial blooms in shallow plateau lake. Ecol. Indic. 153, 110394. https://doi.org/10.1016/j.ecolind.2023.110394.

Wehner, B., Wiedensohler, A., 2003. Long term measurements of submicrometer urban aerosols: statistical analysis for correlations with meteorological conditions and trace gases. Atmos. Chem. Phys. 3 (3), 867–879. https://doi.org/10.5194/acp-3-867-2003.

Zhang, Y., Dai, J., Li, Q., Chen, T., Mu, J., Brasseur, G., Wang, T., Xue, L., 2023. Biogenic volatile organic compounds enhance ozone production and complicate control efforts: Insights from long-term observations in Hong Kong. Atmos. Environ. 309, 119917. https://doi.org/10.1016/j.atmosenv.2023.119917.

Zhong, S., Qian, Y., Sarangi, C., Zhao, C., Leung, R., Wang, H., Yan, H., Yang, T., Yang, B., 2018. Urbanization effect on winter haze in the Yangtze River Delta region of China. Geophys. Res. Lett. 45 (13), 6710–6718. https://doi.org/10.1029/2018GL077239.

Ziadé, N., Bouzamel, M., Mrad-Nakhlé, M., Abi Karam, G., Hmamouchi, I., Abouqal, R., Farah, W., 2021. Prospective correlational time-series analysis of the influence of weather and air pollution on joint pain in chronic rheumatic diseases. Clin. Rheumatol. 40, 3929–3940. https://doi.org/10.1007/s10067-021-05735-2.

Zittis, G., Almazroui, M., Alpert, P., Ciais, P., Cramer, W., Dahdal, Y., Fnais, M., Francis, D., Hadjinicolaou, P., Howari, F., Jrrar, A., Kaskaoutis, D.G., Kulmala, M., Lazoglou, G., Mihalopoulos, N., Lin, X., Rudich, Y., Sciare, J., Stenchikov, G., Xoplaki, E., Lelieveld, J., 2022. Climate change and weather extremes in the Eastern Mediterranean and Middle East. Rev. Geophys. 60 (3). https://doi.org/10.1029/2021RG000762 e2021RG000762.